

## Native gold enrichment process during growth of chalcopyrite-lined conduits within a modern hydrothermal chimney (Manus Basin, PNG)

SI-YU HU<sup>1,\*</sup>, STEPHEN J. BARNES<sup>1,†</sup>, ANAIS PAGÈS<sup>1,2</sup>, MICHAEL VERRALL<sup>1</sup>, JOANNA PARR<sup>3</sup>,  
ZAKARIA QUADIR<sup>4</sup>, LOUISE SCHONEVELD<sup>1</sup>, AND RAY BINNS<sup>3</sup>

<sup>1</sup>CSIRO Mineral Resources, Kensington, Western Australia, 6151, Australia

<sup>2</sup>Department of Water and Environmental Regulation, Joondalup, Western Australia, 6027, Australia

<sup>3</sup>CSIRO Mineral Resources, Lindfield, New South Wales, 2070, Australia

<sup>4</sup>Microscopy and Microanalysis Facility, John de Laeter Centre, Curtin University, GPO Box U1987, Perth, Western Australia 6102, Australia

### ABSTRACT

Seafloor hydrothermal chimneys from back-arc basins are important hosts for metals such as Cu, Zn, Pb, Ag, and Au. Although the general growth history of chimneys has been well documented, recent studies have revealed that the fine-scale mineralogy can be highly complex and reflects variable physicochemical conditions of formation. This study utilized a novel combination of scanning electron microscopy (SEM)-based electron backscattered diffraction (EBSD) and synchrotron X-ray fluorescence microscopy (SXFM) to uncover the detailed growth processes of multiple chalcopyrite-lined conduits within a modern chalcopyrite-sphalerite chimney from Manus Basin and to assess the controls on native gold precipitation. On the basis of previous studies, the chimney conduit was thought to develop from an initial sulfate-dominated wall, which was subsequently dissolved and replaced by sphalerite and chalcopyrite during gradual mixing of hydrothermal fluids and seawater. During this process, sphalerite was epitaxially overgrown by chalcopyrite. Accretionary growth of chalcopyrite onto this early formed substrate thickened the chimney walls by bi-directional growth inward and outward from the original tube wall, also enclosing the outgrown pyrite cluster. A group of similar conduits with slightly different mineral assemblages continued to form in the vicinity of the main conduit during the further fluid mixing process. Four types of distinct native gold-sulfide/sulfosalts associations were developed during the varying mixing of hydrothermal fluids and seawater. Previously unobserved chains of gold nanoparticles occur at the boundary of early sphalerite and chalcopyrite, distinct from gold observed in massive sphalerite as identified in other studies. These observations provide baseline data in a well-preserved modern system for studies of enrichment mechanisms of native gold in hydrothermal chimneys. Furthermore, native gold is relatively rarely observed in chalcopyrite-lined conduit walls. Our observations imply that: (1) native gold is closely associated with various sulfides/sulfosalts in chalcopyrite-lined conduit walls rather than limited to the association with tennantite, Bi-rich minerals, and bornite as reported previously; and (2) the broad spectrum of gold occurrence in chalcopyrite-lined conduits is likely to be determined by the various mixing process between hot hydrothermal fluids with surrounding fluids or seawater. Quantitative modeling of fluid mixing processes is recommended in the future to probe the precise gold deposition stages to efficiently locate gold in modern hydrothermal chimneys.

**Keywords:** Seafloor hydrothermal chimneys, gold, sulfides, fluid mixing, EBSD, synchrotron XFM

### INTRODUCTION

Modern hydrothermal sulfide chimneys, also known as “black smokers,” formed by rapid mixing between hot hydrothermal fluids and cold seawater, have been discovered on the seafloor in various tectonic settings, including oceanic spreading ridges of various spreading rates, arcs, back-arc basins, as well as hotspots (e.g., Haymon 1983; Rona et al. 1986; Haymon et al. 1991; Koski et al. 1994; Binns et al. 1995; de Ronde et al. 2005; Hannington et al. 2005; Tao et al. 2012; German and Seyfried 2014; Petersen et al. 2018). Those sulfide chimneys have a characteristic mineral zonation from external walls dominated by sulfates and iron-oxyhydroxides to sulfide-rich interiors (e.g., Haymon 1983; Koski

et al. 1994; Butler and Nesbitt 1999; Berkenbosch et al. 2012). Extensive previous studies have demonstrated that a typical chimney grows with an initial sulfate (anhydrite, barite, or gypsum) external wall, which then segregates warm hydrothermal fluids from the cold seawater and enhances the further precipitation of sulfides into the pores of the wall and the interior orifice. The hot hydrothermal fluids migrate outward through the wall causing the expansion of chimney structure laterally (e.g., Haymon and Kastner 1981; Haymon 1983; Koski et al. 1994; Nozaki et al. 2016). The model has been complemented by subsequent detailed descriptions of various chimney morphologies, mineral assemblages and trace element enrichment patterns (e.g., Kristall et al. 2006, 2011; Berkenbosch et al. 2012; Binns 2014; Dekov et al. 2016).

Sulfide chimneys from arcs and back-arc basins are important hosts for base metals, such as Cu, Zn, and Pb, and precious metals

\* E-mail: siyu.hu@csiro.au. Orcid 0000-0003-2247-2132

† Orcid 0000-0002-4912-9177

(Au and Ag) (Binns and Scott 1993; Herzig et al. 1993; Herzig and Hannington 1995; Moss and Scott 2001; de Ronde et al. 2003; Fuchs et al. 2019) and some of those, such as the seafloor massive sulfides in the Manus Basin, have attracted interest as targets for deep sea mining (Gena 2013). Understanding the deportment of precious metals in sulfide chimneys can provide significant guidance for the processing and exploration of ancient VMS deposits and deep-sea mining (Petersen et al. 2018; Fuchs et al. 2019). Previous studies have shown that native gold occurs with a wide range of minerals, which include, but is not limited to, chalcopyrite, Bi-telluride, sphalerite, pyrite, tennantite, bornite, and covellite. Gold precipitation mechanisms have been attributed to various factors, including hydrothermal fluids mixing with seawater, conductive cooling, boiling, dissolution, and reprecipitation from hydrothermal reworking; this topic has been reviewed in detail by Fuchs et al. (2019).

In previous studies, conventional whole-rock geochemistry and optical and electron microscopy have been used to unravel associations between Au and other elements within the hydrothermal chimneys (e.g., Herzig et al. 1993; Koski et al. 1994; Moss and Scott 2001). Detailed studies have revealed that the micrometer-scale mineralogy is highly complex, with individual minerals within the same zone presenting various morphologies and having formed under variable physicochemical conditions or having experienced recrystallization (Kristall et al. 2011; Berkenbosch et al. 2012, 2019; Wohlgemuth-Ueberwasser et al. 2015). The links between the fine-scale chimney growth process and local controls of gold precipitation have not hitherto been fully explored. The present study uses a novel combination of high-resolution analytical techniques, synchrotron X-ray fluorescence microscopy (SXFM) and scanning electron microscopy (SEM)-based electron backscattered diffraction (EBSD), to document the microenvironment within a complex chimney that contains several coexisting conduits and native gold. The prime objective is to provide a basis for understanding the local controls for gold precipitation during the deposition of sulfides and sulfosalt in chalcopyrite-lined conduits in a well-understood modern ore-forming setting.

The SXFM is a cutting-edge technique that can provide high-resolution (2  $\mu\text{m}$  scale) maps showing the distribution of a wide range of major and trace elements over centimeter-scale geological samples without destroying samples (e.g., Fisher et al. 2015; Hu et al. 2016; Berkenbosch et al. 2019). Regions of interest are further analyzed via EBSD, a SEM-based technique that has been widely used to image crystal orientations (e.g., Freitag et al. 2004; Barrie et al. 2010; Pearce et al. 2013). The microstructural features of crystals can be used to interpret robust mineral growth sequences at micro- to nano-scale that cannot be observed with an optical microscopy and SEM. This technique has only been recently applied to study the microstructural features of sulfides in chimneys, which has delivered new insights into chimney growth history (Yeats et al. 2017; Hu et al. 2019; Glenn et al. 2020). In this study, we undertook the first detailed microstructural investigations of gold-rich chalcopyrite-lined conduits collected from the Manus Basin by applying a combination of SXFM, SEM-BSE, and EBSD imaging analysis to examine the mineralogical features of multiple conduits and native gold distribution. This study deciphers the mineral association and deposition sequence in the conduits, reconstructs the detailed growth processes of conduits, and assesses the mechanisms of local native gold deposition.

## GEOLOGICAL BACKGROUND

The Manus Basin is situated within the northeastern Bismarck Sea, Papua New Guinea, and comprises the Bismarck and Solomon microplates. It is located within a complex convergence zone between the Pacific and Australian Plates, including active extension regions, transform faults, and active volcanic centers (Fig. 1; Martinez and Taylor 1996). The Manus Basin is an active back-arc basin with spreading rates up to 137 mm/year at the Manus spreading center (Tregoning 2002), resulting from the subduction of the Solomon microplate beneath the Bismarck microplate along the New Britain Trench (Taylor 1979; Davies et al. 1987; Martinez and Taylor 1996). The eastern Manus Basin (EMB) is an extensional transform zone bounded by the Djaul and Weitin faults and consists of neovolcanic edifices (Martinez

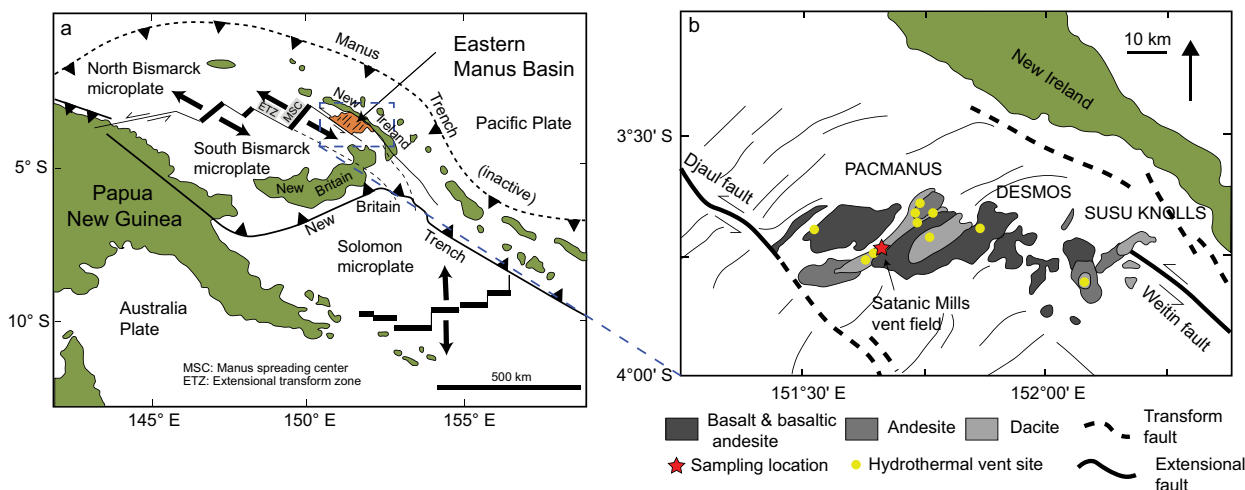


**FIGURE 1.** (a) Geologic setting of the eastern Manus Basin. (b) Sampling location, distribution of hydrothermal vent fields and sites and volcanic edifices ranging from basalt to rhyodacite. Figures are modified from Binns and Scott (1993). (Color online.)

and Taylor 1996). The volcanic edifices range from rhyodacite and dacite to andesite and basalt, which present similar geochemical features to the arc volcanos of the New Britain islands (Kamenetsky et al. 2001). Three major hydrothermal vent fields have developed in the EMB, i.e., the Papua New Guinea–Australia–Canada–Manus Basin (PACMANUS), Desmos, and SuSu Knolls (e.g., Binns et al. 1995, 2007).

The PACMANUS hydrothermal field is hosted by the neovolcanic Paul Ridge (Binns and Scott 1993). Paul Ridge is around 35 km long with a height of 500–700 m above the seafloor and is mainly composed of dacites-rhyodacites. Numerous small, distinct hydrothermal vent sites are developed within the PACMANUS hydrothermal field, including Roger’s Ruins, Roman Ruins, Snowcap, Tsukushi, Satanic Mills, and Fenway vent sites. The Satanic Mills vent site, where the studied chimney was collected, is around 200 m in diameter and 1650 m below sea level. Venting fluids are high temperature (up to 295 °C), acidic with pH of 2–4, and are enriched in Fe, Mn, Cu, Zn, and H<sub>2</sub>S (Reeves et al. 2011). The chimneys in this vent site are either single-spined or multiple-spined with multiple chalcopyrite-lined conduits and mainly consist of chalcopyrite, sphalerite, pyrite, and barite with minor sulfosalt (Pašava et al. 2004; Reeves et al. 2014; Hu et al. 2019, 2020; Meier et al. 2019).

## METHODS

### Sample information and preparation

The analyzed sample is part of a polymetallic chimney fragment with multiple conduits (sample ID: 118584) (Fig. 2). The chimney fragment has been described in detail by Hu et al. (2019). The fragment representing a typical multiple-conduits sulfide chimney was obtained by dredging from the Satanic Mills hydrothermal vent site in 1993 (Hu et al. 2019) and has been stored in the rock store at the Australian Resources Research Center at room temperature. This sample is characterized by multiple sub-parallel chalcopyrite-lined conduits that are surrounded by chalcopyrite-sphalerite transition zones that pass into a sphalerite-dominated outer zone with variable barite and then mantled by Fe-oxide surface (Fig. 2a) (Hu et al. 2019). It was chosen as a well-characterized example of a typical PACMANUS chimney, based on extensive investigation of the area over ten years of investigation since the original discovery of the field by a team led by the Commonwealth Scientific and Industrial Research Organization (CSIRO) since 1991.

A sub-sample (118584-K5) was taken from a part of the chimney fragment and made into a thin section (Fig. 2b) and a corresponding polished mount. The sub-sample comprises multiple chalcopyrite-lined conduits ranging from elliptical to

irregular shape, overgrown by sphalerite and a small amount of pyrite, which then grade into dendritic sphalerite-dominated zones containing fine-grained chalcopyrite. Rosette-shaped barite is observed across the whole section, indicating pervasive seawater ingress. The mineralogical associations resemble the observations on the hand-specimen scale. The study focuses on the development of multiple native-gold-bearing micro-conduits at a thin-section scale; however, the gold-sulfide associations were also observed (based on SEM observations) in other regions of the same chimney, as well as other chimneys from different venting sites (Rogers Ruins and Suzette venting sites) in Manus Basin (Online Materials<sup>1</sup> Figs. S1 and S2). Based on the broader set of investigations of the field, we are confident that the sample chosen for this study is typical and representative of the eastern Manus Basin.

### SEM-EBSD

Mineralogical observations were conducted using an optical microscope (Nikon LV100Pol) and a Phillips XL 40 Controlled Pressure SEM with an energy-dispersive X-ray spectrometer (SEM-EDS) at CSIRO Mineral Resources (Perth, Australia). The backscatter electron (BSE) images were collected at a 30 kV voltage with a beam intensity of ~10 nA and a working distance of 12.5 mm. Areas of interest were further mapped using an EBSD detector (Oxford instrument symmetry) on a Zeiss Ultra Plus Field Emission SEM at CSIRO Mineral Resources and a TESCAN MIRA3 Variable Pressure Field Emission at Curtin University (Perth, Australia). Prior to the analysis, to remove the surface damage caused by mechanical polishing, the mount was re-polished with colloidal silica for one hour and then coated with a thin carbon layer (~5 nm). A 20 kV accelerating voltage and a 120 µm aperture with probe current of 12 nA were used during EBSD data collection. The sample was tilted to 70° during the mapping. The maps contain 1024 × 884 pixels, with a step size of 0.02 to 0.8 µm.

Electron backscatter diffraction mapping (EBSD) uses electron diffraction induced by an electron beam on polished mineral surfaces to map the crystallographic orientation of the crystal lattice at the micro-nano scale within individual grains over areas of several mm<sup>2</sup> (Maitland and Sitzman 2007). Data are presented as a series of different types of maps. Pattern quality maps, showing the spatial distribution of intensity of diffraction patterns, can effectively display the distribution of crystal boundaries, microstructural features within crystals, such as deformation-induced sub-grains (Barrie et al. 2009, 2010). Phase maps can show the spatial distribution of minerals based on indexing of the EBSD patterns. During the analysis, EBSD patterns and energy-dispersive X-ray spectroscopic (EDS) elemental maps were collected simultaneously. In studied samples, gold, chalcopyrite, pyrite and sphalerite have a similar crystal structure, i.e., cubic with similar unit-cell parameters, such that elemental distribution maps of Au, Cu, and Zn based on EDS analysis were needed to supplement the EBSD images to generate maps of phase distributions. This technique has been described in numerous publications, including Maitland and Sitzman (2007), Barrie et al. (2010), and Hu et al. (2019).

### SXFM

SXFM analysis was performed on the XRF microscopy beamline at the Australian Synchrotron (Clayton, Melbourne, Australia). This beamline is coupled with a Kirkpatrick–Baez mirror microprobe end-station, providing a monochromatic 2 µm

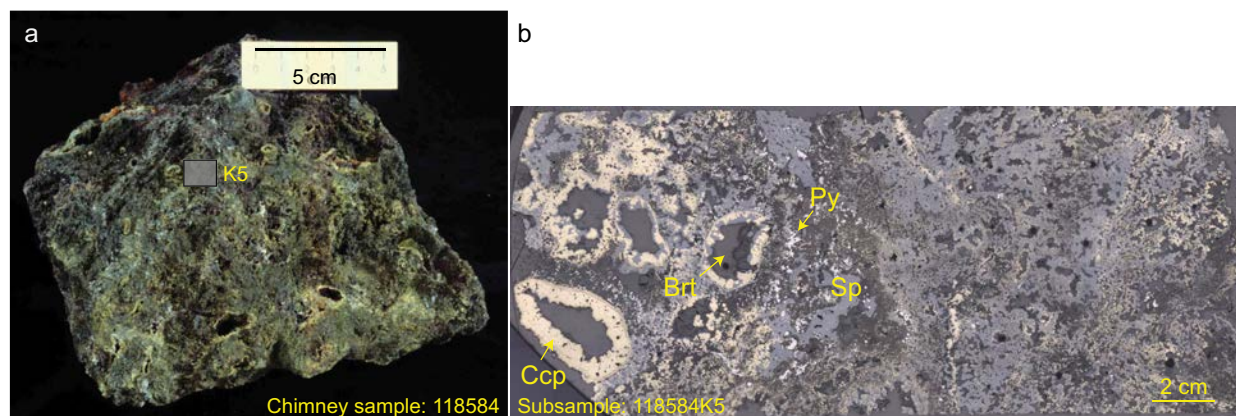


**FIGURE 2.** (a) Optical photograph of the studied polymetallic chimney fragment. (b) Optical photomicrograph (reflected light) of the studied thin section from the fragment, displaying the distribution of multiple chalcopyrite (Ccp)-lined conduits, coarse-grained and dendritic sphalerite (Sp) with dispersed pyrite (Py) and barite (Brt). (Color online.)



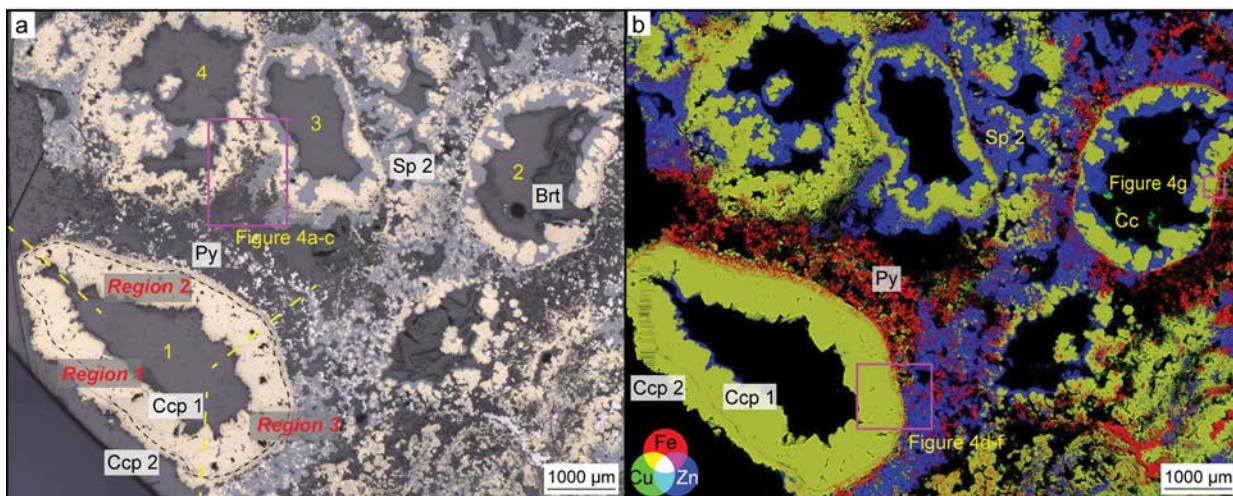


**FIGURE 3.** (a) Optical microscopic image (reflected light) of multiple conduits (left half of Fig. 2b) and (b) the corresponding SXFM red (Fe)-green (Cu)-blue (Zn) composite image showing the distribution of sulfides (chalcopyrite, pyrite, sphalerite, and chalcocite) and barite. The conduits are lined with chalcopyrite, which is displayed as yellow (a) and bright yellow (b). There is a gap separating two generations of chalcopyrite (as Ccp 1 and 2), indicated by the dashed line (a) and directly visible (b). Some chalcopyrite conduits are rimmed by clustered pyrite, which is present as white color in a and red in b. Late-stage sphalerite (as Sp 2) and barite overgrow pre-existing sulfides. Sphalerite is displayed as gray in a and blue in b. Barite is transparent in a, but not visible in b. Chalcocite is shown as bright green in conduits 2 and 3 in b. The conduit 1 is further divided into regions 1, 2, and 3 with the boundaries highlighted with yellow dashed lines in a (lower left). Abbreviations: Ccp = chalcopyrite; Py = pyrite; Sp = sphalerite; Brt = barite; Cc = chalcocite. (Color online.)

beam spot size for energies in the range of 4–20 keV, and equipped with a Maia 384 large solid angle detector array and an integrated real-time processor (Paterson et al. 2011; Ryan et al. 2013, 2014). The sample was scanned at a beam energy of 18.5 keV and a spot size of 2  $\mu\text{m}$  from 384 detectors simultaneously over an area of  $1 \times 0.7$  cm with count rates of  $\sim 4$ –10 M/s and an energy resolution of 300–400 eV (Ryan et al. 2014). Standard foils of Fe, Mn, Pt, and YF3 (yttrium fluoride) were analyzed daily for calculation and calibration of the X-ray flux. The collected spectra were further processed using the GeoPIXE software. Spectra were fitted using yield files, which are calculated based on the mineral assemblage present. Elemental maps were generated using the dynamic analysis methods, which were described in detail in Ryan et al. (2010a, 2010b) and Fisher et al. (2015).

## RESULTS: PETROGRAPHIC OBSERVATIONS

### Overview of the sub-sample

The sub-sample includes four sulfide-lined hollow tubes, referred to hereafter as conduits, that are ellipsoidal, sub-ellipsoidal, and irregular (labeled as 1 to 4 in Fig. 3). The wall of each conduit is lined with coarse-grained chalcopyrite, entirely or partly overgrown by late-stage sphalerite. Conduits 1 and 2 are rimmed by fine-grained clustered pyrite and chalcopyrite growing into the interstitial space between the conduits (Fig. 3). In conduit 1, a gap (indicated in Fig. 3a and directly visible in Fig. 3b) separates chalcopyrite into two groups, labeled as chalcopyrite 1 (Ccp 1) and 2 (Ccp 2). The gap is not observed in other conduits. The external walls of conduits 3 and 4 are characterized by chalcopyrite showing a transition from dendritic structure to clusters of coarse-grained and euhedral crystals from the exterior to the interior of the conduit (Figs. 4a–4c). Minor pyrite is included in the dendritic texture (Fig. 4c). Accessory minerals in this sub-sample include galena, barite, tennantite, and chalcocite (Figs. 3 and 4). Native gold is observed in close associations with various sulfides and sulfosalts in the chalcopyrite-dominated wall (e.g., Figs. 4d–4g), and this will be described in detail in the following text.

### Conduit 1

This conduit is described in detail as it exemplifies the critical features found in all the conduits. For purposes of description, conduit 1 is further divided into regions 1, 2, and 3 (Fig. 3a) based on the occurrence of clustered pyrite and late-stage sphalerite. The conduit is also divided into four distinguishable zones from the interior to the exterior; these zones and the relationship between them are exemplified in the specific regions illustrated in Figure 5. The term “region” refers to a specific area of conduit 1, as delineated in Figure 3a, while the term “zone” denotes concentric, mineralogical features that can be recognized in multiple conduits (Fig. 5). The main characteristics and associations between regions and zones are summarized in Table 1.

From interior to exterior, zone 1 is the closest to the interior conduit void and mainly consists of coarse-grained Ccp 1; zone 2 is relatively porous and corresponds to the narrow gap between Ccp 1 and Ccp 2 in Figure 3; zone 3 includes pyrite that is overgrown by coarse-grained Ccp 2, and zone 4 consists of dispersed pyrite overgrown by Ccp 2 and then sometimes further rimmed by late-stage sphalerite (as Sp 2). Region 1 (Fig. 5a) includes zones 1, 2, and 3, while region 2 (Fig. 5b) includes zones 1, 2, 3, and 4 without late-stage Sp 2; and region 3 (Fig. 5c) includes zones 1, 2, 3, and 4 with late-stage Sp 2. Regions 1 and 3 representing two end-members of petrographic features are described in detail, with region 2 being gradational between them.

The main difference between regions 1 and 3 is the proportion of various sulfides and porosity in zones 2 and 3. In region 1, zone 2 is dominated by sphalerite (as Sp 1), sandwiched by both Ccp 1 and 2. In BSE images, Sp 1 occurs as homogeneous patches and contains some voids (Figs. 5d–5f). Euhedral pyrite occurs on the boundary of zones 2 and 3 and is overgrown by Ccp 2 in zone 3

(Figs. 5d and 5g). By contrast, zone 2 in region 3 is more porous, and contains approximately 10% Sp 1 that is unevenly distributed in smaller patches (up to 30  $\mu\text{m}$ ) that rim voids (Figs. 5h and 5i). The thickness (from interior to exterior) of zone 3 varies from more than 100  $\mu\text{m}$  in region 1 to 50–100  $\mu\text{m}$  in region 3.

### Native gold

Four types of associations between gold and sulfide/sulfosalt are observed within the conduits. Individual gold grains are generally sub-rounded and <1  $\mu\text{m}$ . Gold particles occur on the surface of triangular tennantite within Ccp 1, which is observed in all the conduits and is defined as Tt-associated gold (Fig. 4g). Gold that exclusively follows the boundary between Sp 1 and Ccp is denoted by Sp-associated gold and occurs as continuous chains (Figs. 5e and 5f) or as discrete grains (Fig. 5g). Similar observations are also made in other chimneys where sphalerite is sandwiched between chalcopyrite (Online Materials<sup>1</sup> Fig. S1). Py-associated gold occurs on the boundaries of, or within, the euhedral pyrite (Fig. 5g). The cluster of gold nanoparticles that occurs in chalcopyrite without the presence of Sp 1 in porous zone 2 (Figs. 5h and 5i) is defined as Ccp-associated gold. This association is common in other chalcopyrite-only conduits in other chimneys (e.g., Online Materials<sup>1</sup> Fig. S2).

## RESULTS: MICROSTRUCTURAL FEATURES

Pattern quality maps are grayscale maps showing variations in diffraction pattern contrasts. Grain boundaries and sub-grain boundaries appear as gray lines because they are poorly crystalline and therefore do not produce distinct diffraction patterns, whereas uniform areas indicate interiors of uniform crystals. Coupled with the coincident EDS measurements, the maps show grain size, shape, and distribution of phases even where it is difficult to tell crystal structures apart. The maps, therefore, provide a better understanding of the paragenesis, which cannot be easily recognized via other microscopic techniques. The pattern quality maps within region 1 and 3 are herewith described to highlight the microstructural features of conduit 1.

### Region 1

Zones 1 and 3 consist of coarse-grained chalcopyrite grains that, in contrast to the homogenous crystals shown in the BSE image (Fig. 6a), range in size and morphology. Ccp 1 and 2 vary from ~10  $\mu\text{m}$  anhedral crystals close to zone 2 to elongated crystals (~100  $\mu\text{m}$ ) that extend both toward the conduit axis in zone 1 and outward into the inter-conduit space in zone 3, respectively (Fig. 6b). Both morphologic varieties of crystals lack preferred

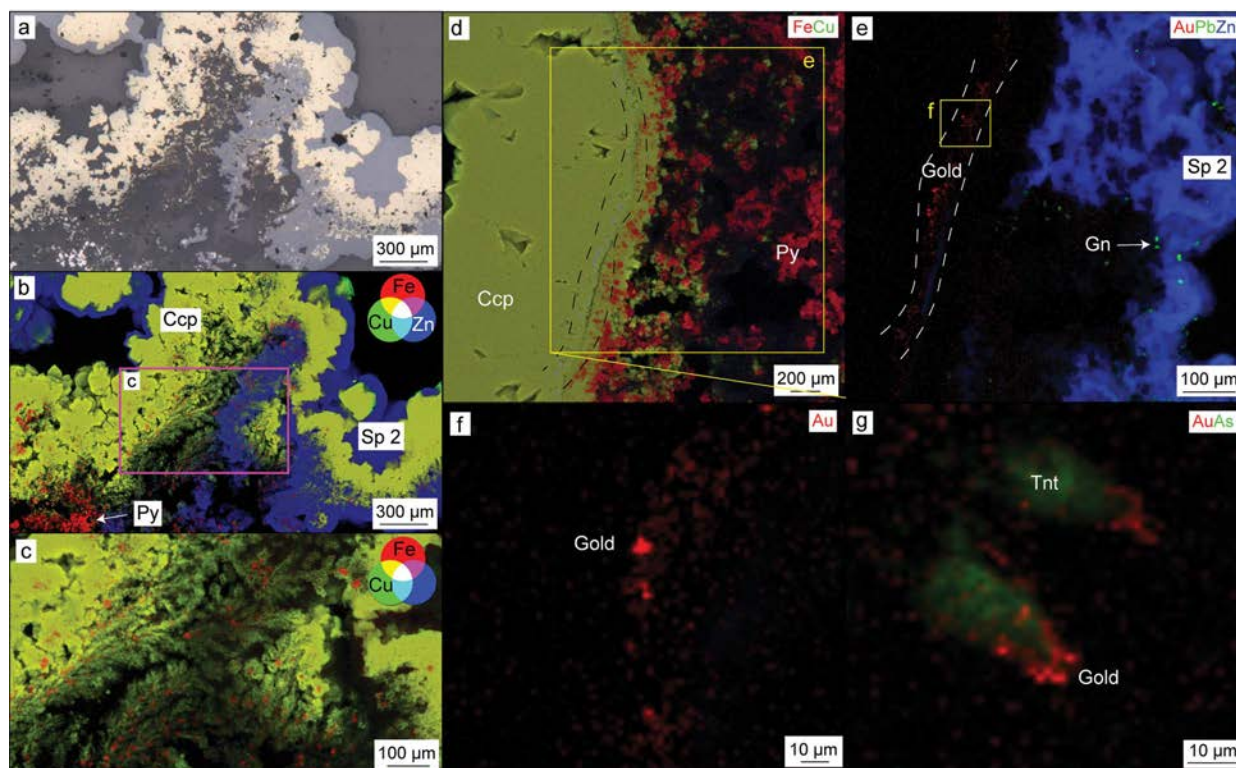


**FIGURE 4.** (a–c) Chalcopyrite varying from dendrite to euhedral and overgrown by sphalerite. (a) Optical microscopic image in reflected light. (b) The corresponding SXFM image showing the dendrite structure not visible in a, without (left part) and with (right part) overgrowth by sphalerite. Due to the depth penetration of synchrotron X-ray, the features are present clearly in three dimensions. (c) Higher magnification observation of the dendrite from b showing pyrite grains are enclosed within the dendritic structure. (d–f) SXFM elemental maps showing the distribution of gold. (d) Clustered pyrite rims chalcopyrite boundaries. (e) Gold in chalcopyrite conduits and galena within later stage sphalerite from the box in d; (f) Higher magnification observation of gold from e; (g) Native gold is associated with tennantite from Figure 3b. Abbreviations: Ccp = chalcopyrite; Sp = sphalerite; Py = pyrite; Gn = galena; Tnt = tennantite. (Color online.)



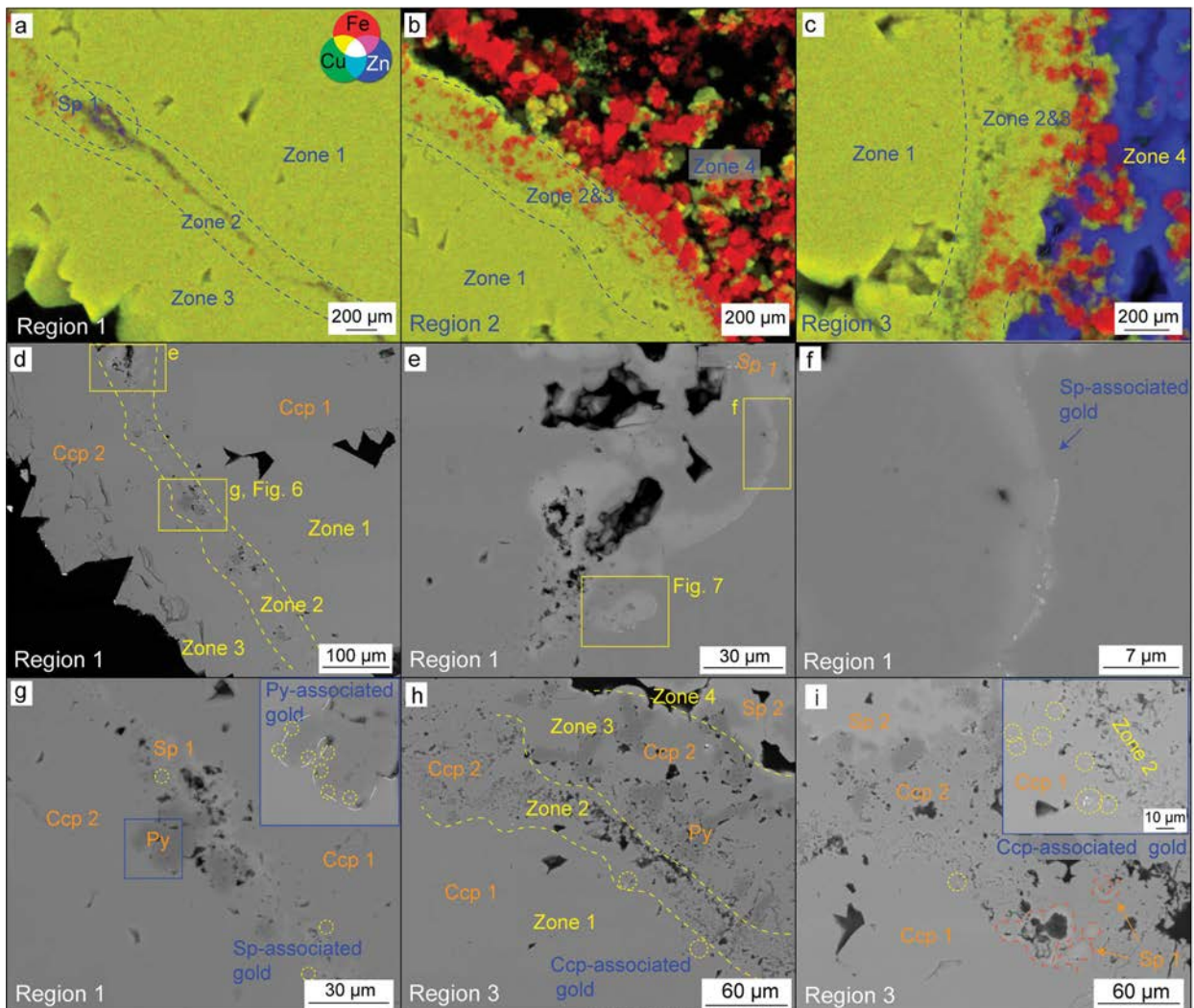


**FIGURE 5.** (a–c) SXFM elemental maps of region 1–3, showing the distribution of chalcopyrite (Ccp, in yellow), pyrite (Py, in red), and sphalerite (Sp, in blue) and defining the concentric zones that are identifiable in each region. Region 1 is dominated by chalcopyrite with a few sphalerite and pyrite grains. Region 2 is characterized by chalcopyrite overgrown by disseminated pyrite. Region 3 contains similar features to those in region 2 and also shows overgrowth by a late-stage sphalerite. (d–g) SEM-BSE images of region 1, including zones 1–3. Zone 1 consists of chalcopyrite (Ccp 1). Zone 2 features a thin layer of sphalerite (Sp 1). In zone 3, pyrite (Py) grows within chalcopyrite (Ccp 2). (d) Region 1 containing zones 1–3. (e) Gold chains delineating the boundary of Sp 1 and Ccp 1. (f) High magnification observation from e. (g) Euhedral pyrite growing into Ccp 2 from Sp 1. The insert shows gold distribution over the pyrite. (h–i) SEM-BSE images of region 3. (h) Region 3 containing zones 1–4. Zones 1 and 3 share similar features to those in region 1. Zone 2 is more porous and a late-stage sphalerite forms zone 4. (i) High magnification observation of zone 2, showing this zone contains voids rimmed by Sp 1 (delineated by orange dashed lines) and chalcopyrite-associated gold. Insert: Ccp-associated gold. Gold grains are circled with yellow dashed lines. (Color online.)

growth orientations (Online Materials<sup>1</sup> Fig. S3). By contrast, zone 2 is formed mainly by smaller grained crystals, compositionally dominated by Sp 1. The crystal grains are fine (<1 μm), where Sp-associated gold is distributed as discrete grains (Figs. 5f and 6b–6d). Sphalerite that is coated by a gold nanoparticle chain contains larger sphalerite crystal grains (>2 μm) (Figs. 5g, 5h, and 7; Online Material<sup>1</sup> Fig. S4). It is notable that the phase change from Sp 1 to Ccp 1 occurs in a single crystal with gold nanoparticles precipitated on the chemical boundary rather than on the crystal boundary (Figs. 7 and 8). Fine-grained (<1 μm) chalcopyrite crystals are sometimes observed within or surrounding Sp 1 (Figs. 7c and 9b). Pyrite grains appear either euhedral or

polycrystalline (Figs. 6b and 9). Py-associated gold nanoparticles occur on the surface of, or within, pyrite (Fig. 9).

### Region 3

Ccp 1 in zone 1 and Ccp 2 in zone 3 show similar features to those in region 1 (Fig. 10). However, zone 2 is more porous than that in region 1 and is shown as a gap in the large-scale pattern quality map. This zone contains mainly chalcopyrite with minor sphalerite and pyrite (Fig. 11). Pyrite occurs continuously from fine-grained (several micrometers) on the boundary of zones 2–3 to larger euhedral grains (~30 μm) in zone 3, which are then overgrown by euhedral to anhedral Ccp 2 grains and further rimmed

**TABLE 1.** A summary of mineralogical associations in all the zones and regions

Zones	Dominated mineralogy and porosity	Region 1	Region 2	Region 3
Zone 1	Coarse-grained Ccp 1			
Zone 2	±Sp 1, gold-rich, porous	Less porous		More porous and with Sp 1 occasionally observed
Zone 3	Euhedral Py overgrown by Ccp 2	> 100 µm thick		50–100 µm thick
Zone 4	Disseminated Py overgrown by Ccp 2 and ±late-stage Sp 2		Without late-stage Sp 2	With late-stage Sp 2

Notes: The regions refer to the specific areas with various occurrences of clustered pyrite and late-stage sphalerite as delineated in conduit 1 (Fig. 3). The zones represent the concentric mineralogical variations from chimney interior to the exterior (e.g., Fig. 5). Regions including the corresponding zones are highlighted with light green color and the additional unique features of zones are described in each region column. Abbreviations: Ccp = chalcopyrite; Py = pyrite; Sp = sphalerite.

by Sp 2 (Fig. 10c). On the zones 1–2 and zones 2–3 contacts, Ccp show smooth boundaries where small chalcopyrite grains are present (Fig. 11c). Native gold is associated with the cavities along those boundaries (Figs. 4e, 4f, and 11b). Such gold-Ccp association is not observed in region 1.

## DISCUSSION

### Growth of conduit 1

The chimney fragment containing the studied area presents the common zonation features of chalcopyrite-sphalerite-rich chimneys reported in previous studies (e.g., Haymon 1983; Koski et al. 1994; Berkenbosch et al. 2012), and the general growth history of the fragment is consistent with the previous models as described in the Introduction. While most previous studies focused on the single-stemmed chimneys, this study reveals the detailed

growth process of the multiple sub-parallel conduits occurring within the chimney fragment, as well as the local controls of native gold enrichment.

In the studied subsample, the textural features of conduit 1 are common to most of the other conduits. Hence, its growth history provides a good model for the development process of other conduits. The shape of conduit 1 is ellipsoidal, which suggests a focused flow of hydrothermal fluids (Turner and Campbell 1987; Koski et al. 1994). The microstructural maps, optically appearing as homogenous chalcopyrite, show that the wall actually consists of coarse-grained chalcopyrite that varies from anhedral crystals, close to zone 2 (tens of micrometers) to elongated crystals (~hundreds of micrometers) toward the void in zone 1 and outward into the inter-conduit space in zone 3, respectively (Figs. 6 and 10). This increase in crystal size away from zone 2 is indicative of the bi-directional

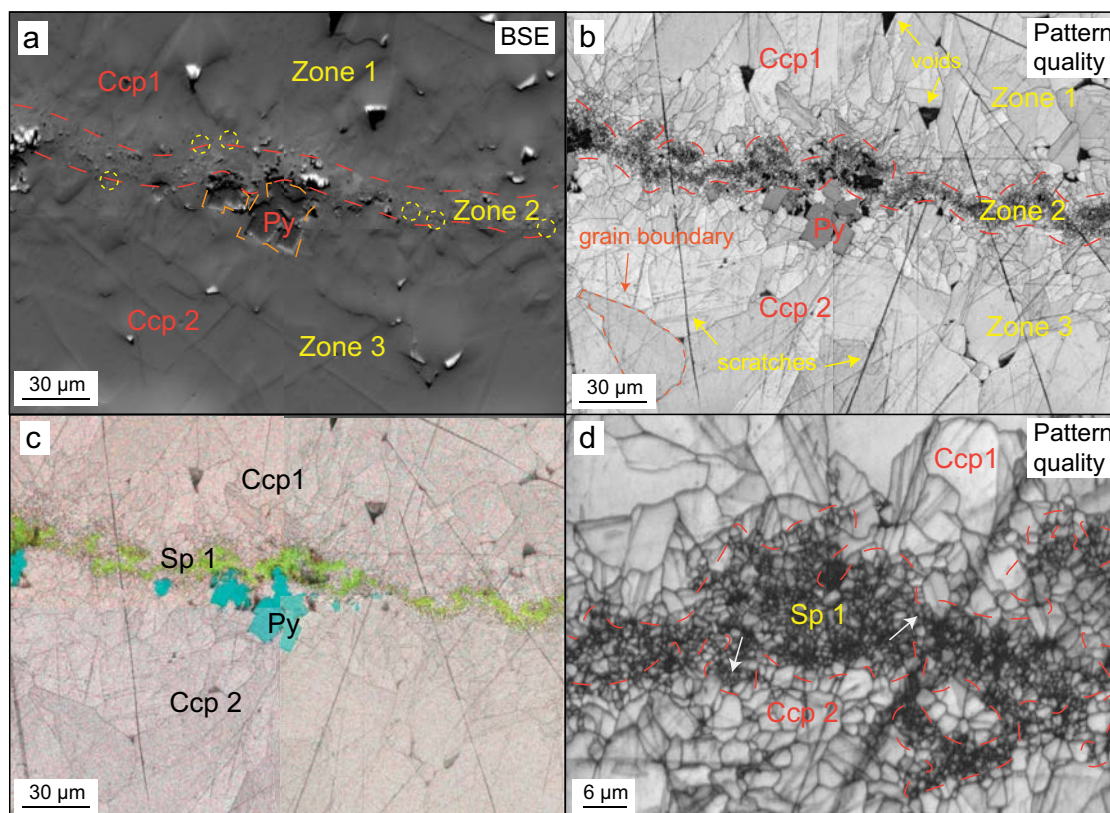


**FIGURE 6.** Microstructural features of region 1. (a) BSE image, (b) pattern quality map, and (c) the pattern quality map overlain with the EDS elemental map, showing the distribution of sphalerite (Sp, bright green), pyrite (Py, sky blue), and chalcopyrite (Ccp, light pink). In the pattern quality maps, the straight and sharp dark lines are scratches introduced by the mechanical polishing during sample preparation. The gray lines indicate grain boundaries, with an example shown in b. (d) High-magnification image of zone 2. The images show that a thin layer of sphalerite separates chalcopyrite into two groups. The sphalerite layer consists of multiple fine-grained crystals, while chalcopyrite varies from fine-grained close to zone 2 to coarse-grained into zone 1 and zone 3, respectively. Euhedral pyrite occurs within chalcopyrite in zone 3. (Color online.)



**FIGURE 7.** Microstructural features of sphalerite patches and the associated gold in region 1. (a) BSE image, (b) pattern quality map; and (c) the pattern quality map overlain with the EDS elemental maps, showing the distribution of sphalerite (Sp 1, yellow), chalcopyrite (Ccp 1, blue) and native gold (bright in a and red in c). The sphalerite patch is homogenous in BSD observation; however, it consists of multiple fine-grained crystals that become larger radially from the center to the boundary. (d) This is from c and shows the pattern quality map of gold nanoparticles (<500 nm, highlighted by yellow circles). The images show that sphalerite (Sp 1) is overgrown by chalcopyrite (Ccp 1), and gold is located on the phase boundary of the two minerals. It is noteworthy that the boundary is indicated by gold distribution and chemical variations rather than by crystal boundaries. (Color online.)

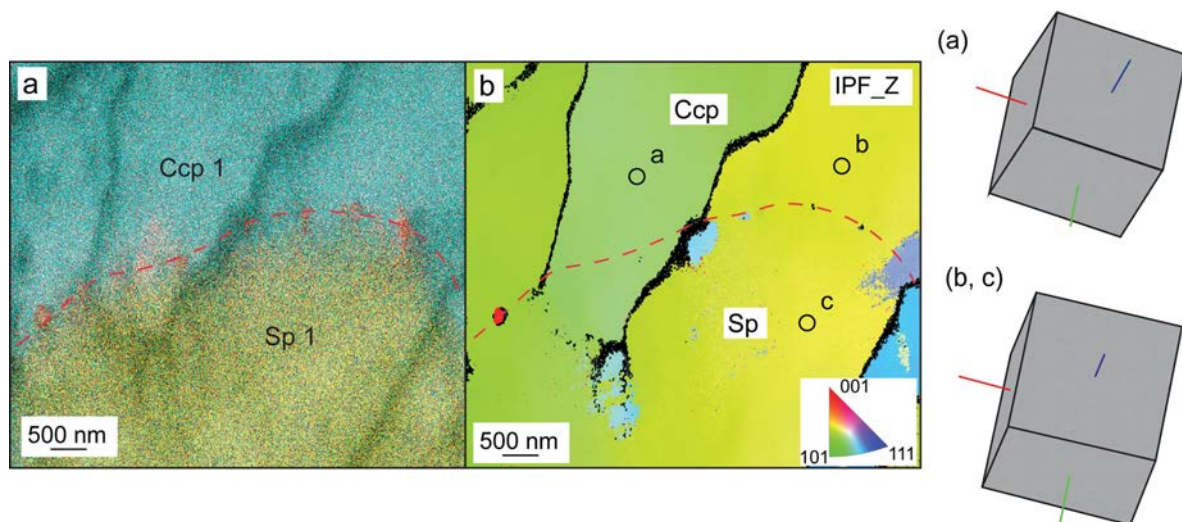
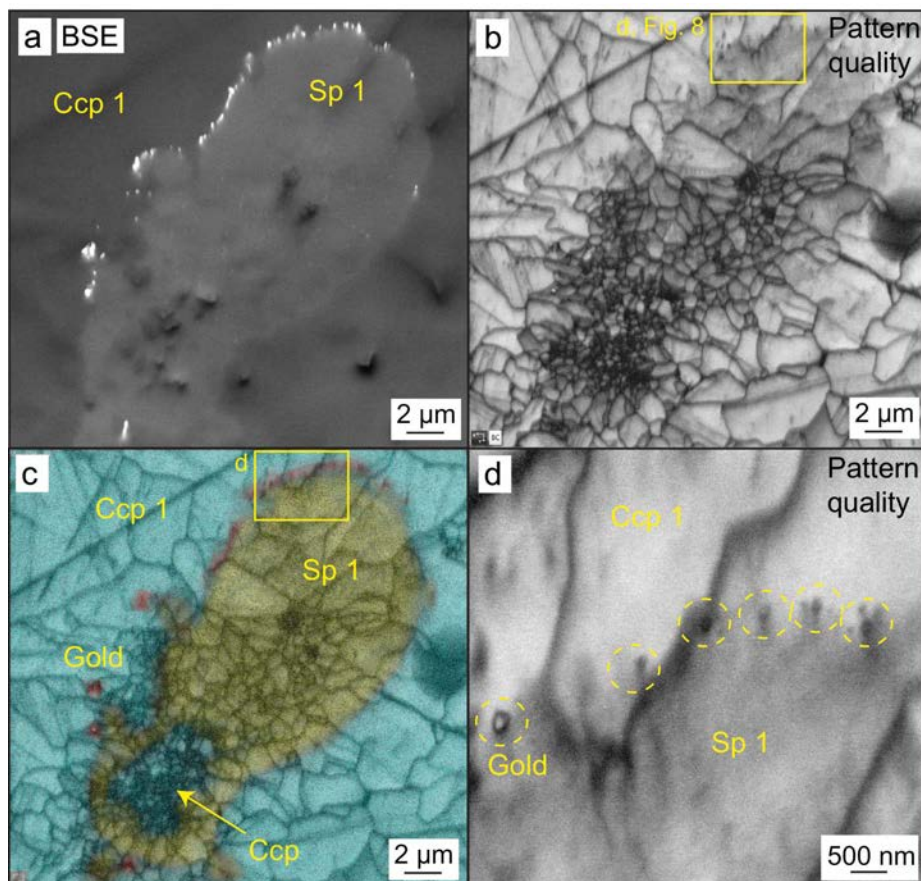


**FIGURE 8.** (a) The pattern quality map overlain with the EDS elemental maps, showing the distribution of sphalerite (Sp 1, yellow), chalcopyrite (Ccp 1, blue), and native gold (red) and (b) inverse pole figure (IPF\_Z) showing crystal lattice orientation in the same area as Figure 7d. The crystal orientations are from points a, b and c in b. In the IPF\_Z map, the orientations parallel to Z direction (the direction normal to the plane of the image) correspond to the crystallographic directions indicated by the color scheme. All the large crystals are yellowish-green, which means the poles to the (101) plane of those crystals are nearly parallel to the Z direction, orthogonal to the page. The inverse pole figures in the X and Y directions show similar features. The boundary between chalcopyrite and sphalerite are delineated with a red dashed line. The image shows that the sphalerite and chalcopyrite grains are epitaxial (i.e., share the same crystal lattice orientation) as there are no grain boundaries between the chemical transition and the lattice orientations of both minerals (points b and c) are the same. There is a slight orientation change across a sub-grain boundary between points a and b, extending through the sphalerite-chalcopyrite phase boundary. Gold (as a red spot) is situated on the boundary. (Color online.)



growth of chalcopyrite, which grows toward and away from the conduit channel as Ccp 1 and 2. During the initial mixing between hot hydrothermal fluids and seawater, sulfates, such as anhydrite and barite, are the early minerals forming the conduit wall while segregating the hot hydrothermal fluids with seawater and are then dissolved and replaced by sulfides when hydrothermal fluids flow away from the channel (Haymon 1983). The bi-directional growth of chalcopyrite, Sp 1-dominated layer, and the outgrown pyrite are most likely to develop from this early substrate.

In detail, conduit 1 comprises three regions with different proportions of clustered pyrite, late-stage Sp 2, various thickness of Ccp 2 and porosity in zone 2 (Fig. 5; Table 1). This sequence is likely to develop through multiple stages with variable degrees of mixing between high-temperature fluids with seawater or the relatively low-temperature surrounding fluids. Region 1 is characteristic of thicker Ccp 2 with large crystals, less clustered pyrite, porous zone 2, and lacks later stage Sp 2 compared to the other regions. Sp 1, which is sandwiched between Ccp 1 and 2, contains fine grains, which occur either on the smooth surface of chalcopyrite (Fig. 6d) or are enclosed by fine chalcopyrite grains (Fig. 9b). This observation resembles the coupled dissolution-reprecipitation (CDR) products in that fine-grained product phases are present on the sharp interface of the parent phases (Putnis 2009; Etschmann et al. 2014; Altree-Williams et al. 2015). If CDR occurs, chalcopyrite is supposed to be replaced by sphalerite. However, in the seafloor hydrothermal systems, such chemical reaction is less likely to occur. The dissolution of chalcopyrite requires a hot ( $T > 260^{\circ}\text{C}$ ) hydrothermal fluid passing through, which reduces the pH simul-

taneously and prevents the precipitation of sphalerite (Fig. 14 in Franklin et al. 2005). Therefore, the replacement of chalcopyrite with sphalerite is not thermodynamically favorable. As such, the CDR mechanism is ruled out. Alternatively, our observations can be explained by the dissolution of chalcopyrite when a hot fluid flows in at the first step, and fine-grained sphalerite and chalcopyrite are precipitated during the conductive cooling or the mixing of the hydrothermal fluid with remaining fluids.

It is notable there is an epitaxial relationship between adjoining sphalerite and chalcopyrite grains, i.e., both minerals share the same lattice orientation. Gold nanoparticles precipitate on the phase boundary in zone 2 (Figs. 7 and 8; Online Materials<sup>1</sup> Fig.S4). This novel finding can only be revealed using EBSD and has not been reported by previous studies, which used only SEM and optical microscopy. Two mechanisms, i.e., mineral replacement and overgrowth, can account for the phase change. Sphalerite is replaced by chalcopyrite during metasomatic reactions, which has been usually applied to interpret the “chalcopyrite disease” in massive sulfide deposits and hydrothermal vents (Barton and Bethke 1987; Kojima and Sugaki 1987; Keith et al. 2014). If the metasomatic reaction occurs, chalcopyrite as the product phase is supposed to be fine-grained compared to the parent phase, i.e., sphalerite in our study (Putnis 2009; Altree-Williams et al. 2015). By contrast, there are no size variations between chalcopyrite and sphalerite (Fig. 7; Online Materials<sup>1</sup> Fig. S4). As such, this mechanism is not supported by our observations. The epitaxial growth of chalcopyrite on sphalerite is alternatively plausible due to the similar lattice spacings of both minerals. This is a

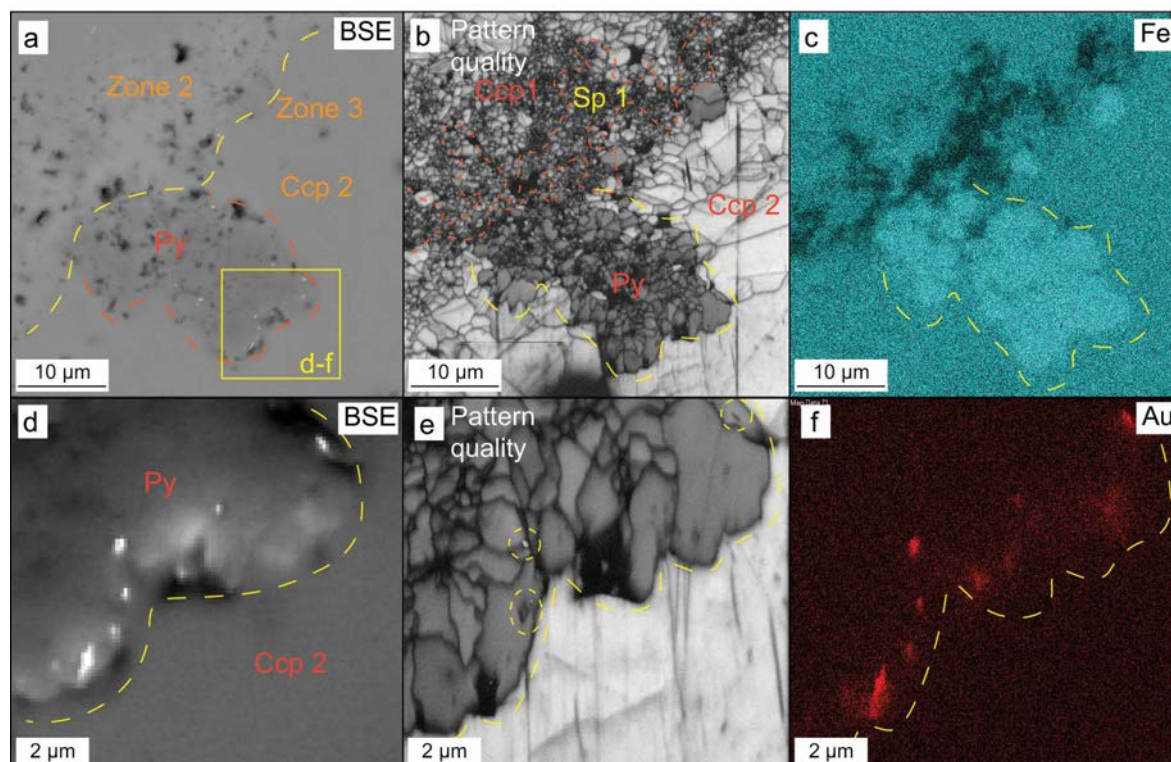


**FIGURE 9.** Microstructural features of pyrite and the associated gold in region 1. (a–c) BSE image, pattern quality map and Fe distribution map showing that pyrite grows from small crystals ( $<1\ \mu\text{m}$ ) in zone 2 to larger ( $\sim 2\ \mu\text{m}$ ) in zone 3 of region 1. (d–f) BSE image, pattern quality map and Au distribution map showing that gold is located within and/or at the boundaries of pyrite grains. (Color online.)

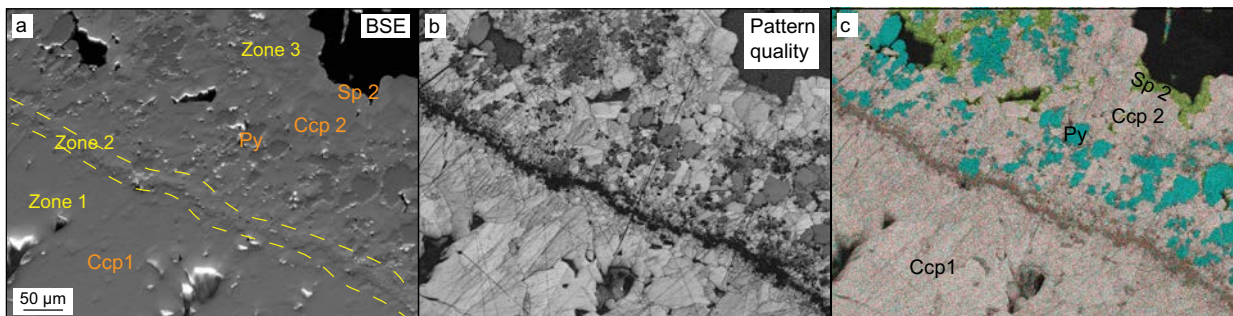
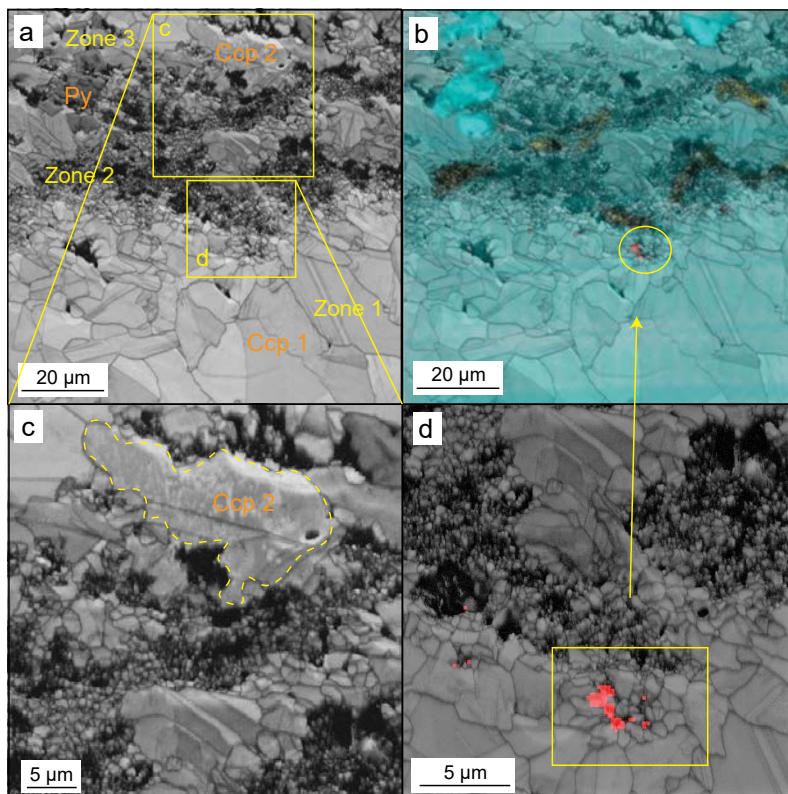


**FIGURE 10.** Microstructural features of region 3. (a) BSE image, (b) pattern quality map, and (c) the pattern quality map overlain with the EDS elemental maps, showing the distribution of pyrite (Py, sky blue), chalcopyrite (Ccp, light pink), and late-stage sphalerite (Sp2, bright green). Similarly, to region 1, chalcopyrite varies from fine-grained close to zone 2 to coarse-grained into zones 1 and 3, respectively. However, zone 2 in region 3 is more porous, present as a dark gap in the large-scale pattern quality map. Pyrite is disseminated within Ccp 2, however, grain size variation from fine close to zone 2 to coarse in zone 3 can be observed. Late-stage sphalerite mantles the pre-existing chalcopyrite and pyrite. (Color online.)

**FIGURE 11.** High magnification observations of zone 2 in region 3. (a) pattern quality map and (b) the pattern quality map overlain with the EDS elemental maps, showing the distribution of gold (in red), sphalerite (in yellow), pyrite (Py) in bright blue and chalcopyrite (Ccp 1 and 2) in light blue. Zone 2 consists of fine-grained sphalerite and chalcopyrite crystals. (c) Enlargement of pattern quality map in the indicated area of (a) showing the sharp boundaries of chalcopyrite. (d) Enlargement of pattern quality map in a showing the smooth boundaries of chalcopyrite. Cavities along the boundaries are filled by small (<2  $\mu\text{m}$ ) particles, including gold. Gold particles in this image are too fine to be revealed via EBSD, but the EDS map has confirmed their presence. (Color online.)



common mineral overgrowth mechanism, for example, the epitaxial growth of arsenian pyrite over As-free pyrite (Deditius et al. 2008). The smooth transition from Sp 1 to Ccp 1 can be formed during the progressive mixing of hydrothermal fluids into seawater when the sulfate wall is dissolved and the sulfide interior wall is built. Instead, the fine-grained chalcopyrite within Sp 1 (Fig. 7c) can be best explained by the coupled dissolution of sphalerite and reprecipitation of chalcopyrite by new hot hydrothermal fluids. Pyrite occurs as euhedral or clusters of fine-grained crystals confined within a similar frame of the euhedral pyrite cluster (Figs. 6a and 9). Those fine-grained crystals are likely to be a consequence of the similar early dissolution and late precipitation process. Our observations imply that the development of conduit 1 involves complex processes, which include initial epitaxial overgrowth of chalcopyrite over sphalerite and dissolution and precipitation of sulfides by new pulses of hydrothermal fluids.

Region 3 includes a narrow Ccp 2, more clustered pyrite, late-stage Sp 1, and porous zone 2. Pyrite grows from fine-grained particles in zone 2 to euhedral crystals in zone 3, which is similar

to the distribution in region 1; however, in region 3 pyrite is more abundant in zone 3, and continues growing into zone 4, then is overgrown by chalcopyrite and late-stage Sp 2 (Fig. 10). Another distinct feature is that on the boundaries of zones 1 and 2, small chalcopyrite grains occur on the smooth edges of large chalcopyrite grains (Fig. 11c). This is similar to the early dissolution and late precipitation mechanism mentioned above; however, if the processes are coupled is unknown. The smooth edge of large chalcopyrite is interpreted to be the result of the influx of hotter Cu-rich hydrothermal fluids. Subsequently, the new fine-grained chalcopyrite is precipitated in supersaturated conditions when the hot hydrothermal fluids contact surrounding fluids. Furthermore,



there are no large Sp 1 patches preserved in region 3. Instead, Sp 1 is less visible in optical observations and only presents as small particles or rimming the cavities in zone 2 (Fig. 5i); these have probably experienced extensive dissolution due to consistent discharging of the hotter fluids.

### Other chimney conduits

Rather than the ellipsoidal shape of the conduit 1, conduit 2 shows less ellipsoidal shape, and conduits 3 and 4 present irregular shapes indicative of forming from less focused venting fluids. Additionally, the boundaries of conduits 3 and 4 are characterized by dendritic chalcopryrite that coalesces into euhedral crystals toward the conduit (Figs. 4a–4c). The dendritic features can only be visualized by SXFM; they are not apparent in optical microscopic images as chalcopryrite appears as fine-grained particles in sphalerite and resin. Such features are the best examples showing the supersaturated conditions during the initial fluid mixing (e.g., Hu et al. 2019). The euhedral crystals can be consequences of either the deposition from saturated venting fluids (e.g., Hu et al. 2019) or recrystallization of immature dendritic textures to a compact massive texture (Wohlgemuth-Ueberwasser et al. 2015). Furthermore, the growth direction of dendritic chalcopryrite into larger grains is consistent with that of fine-grained chalcopryrite and pyrite close by, which grow away from the channel of conduit 1 (Fig. 3b). Therefore, conduits 3 and 4 are possibly formed due to the diffusing of hydrothermal fluids during the expansion of conduit 1, while there is no obvious evidence showing the timing relationship between conduits 1 and 2.

The fine-grained sphalerite (Sp 1) layer is not observed in conduits 2–4. The primary wall of conduit 2 only contains fine-grained pyrite clusters, which grow away from the channel as well. This resembles the pyrite clusters rimming conduit 1. It is possible, but not conclusive, that the pyrite wall of conduit 2 formed simultaneously with pyrite clusters that grew on the initial sulfate layer in conduit 1 when diffused hydrothermal fluids mixed with lower-temperature surrounding fluids. Chalcopryrite continuously grows toward the conduit channel from the pyrite wall that gradually isolates hydrothermal fluids from the surrounding fluids. In contrast to conduits 1 and 2, no such pyrite clusters are observed in conduits 3 and 4. The absence of pyrite clusters and the occurrence of dendritic chalcopryrite are likely to be the result of high formation temperatures, for example, caused by the diffused hydrothermal fluids mixing with only a small amount of low-temperature surrounding fluid, causing chalcopryrite only to precipitate. The occurrence of later stage Sp 2, barite, and chalcocite (Fig. 3) within the conduits suggests a waning stage of chimney growth, e.g., the weakening of hydrothermal fluid flow and the influx of seawater (Janecky and Seyfried 1984; Halbach et al. 1998). Therefore, based on the above discussion, the group of various conduits is developed through multiple stages of mixing between focused/diffused warm hydrothermal fluids and cooler surrounding fluids.

### The deposition mechanisms of native gold

In the studied subsample, four types of gold-sulfide/sulfosalt associations are presented. Gold has been proposed to be transported as Au-bisulfide, Au-chloride complexes, or colloidal nanoparticles in hydrothermal fluids (Benning and Seward 1996; Stefánsson and Seward 2003, 2004; Williams-Jones et al. 2009;

Gartman et al. 2018; Fuchs et al. 2019). The concentrations of Au in venting fluids are extremely low; however, the fluids will become saturated in Au due to the dramatic physicochemical changes within the chimney, resulting in the coexistence of native gold and sulfides in black smokers (Hannington et al. 1991; Herzig et al. 1993; Murphy and Meyer 1998; Moss and Scott 2001; Iizasa et al. 2018). Native gold in hydrothermal chimneys has been observed in association with sphalerite, with Cu-rich minerals such as chalcopryrite, tennantite, and bornite, and with Bi-rich minerals, such as maldonite ( $\text{Au}_2\text{Bi}$ ) (Murphy and Meyer 1998; Moss and Scott 2001; Törmänen and Koski 2005; de Ronde et al. 2011; Berkenbosch et al. 2019). The direct precipitation of primary gold occurs as a result of changes in the physical and chemical properties of hydrothermal fluids, such as temperature drops, pH increases, and oxidation due to seawater-fluid mixing (Hannington et al. 1986; Herzig et al. 1993; Murphy and Meyer 1998; Moss and Scott 2001). Alternatively, gold has been suggested to be scavenged by liquid bismuth from the hydrothermal fluids at later stages of the mineralization (Törmänen and Koski 2005; Berkenbosch et al. 2012). Secondary remobilization of Au can occur due to the later stage processes by oxidation of chalcopryrite, and hydrothermal recrystallization and replacement, resulting in the occurrence of native gold at grain boundaries of Cu-rich sulfides (Hannington et al. 1995). Finally, recent studies showed that the boiling in the subsurface can generate native gold, which is transported as the colloidal form in vent fluids (Gartman et al. 2018; Fuchs et al. 2019; Falkenberg et al. 2021). This mechanism can make a significant contribution to native gold enrichment in hydrothermal chimneys.

In the eastern Manus Basin, six Au complexes, including Au-bisulfide, Au-chloride, and Au-OH complexes, from the venting fluids of the Satanic Mill hydrothermal vent site were evaluated via thermodynamic modeling by Moss and Scott (2001). In their study,  $\text{Au}(\text{HS})^0$  was suggested to be the most stable Au carrier when the temperature of venting fluids is  $<300^\circ\text{C}$  and pH is no more than 4. Moss and Scott (2001) further suggested that multiple factors can contribute to the reduction of  $\text{Au}(\text{HS})^0$  and consequent gold precipitation, including decreased sulfur activity and increased pH and  $f_{\text{O}_2}$  (via sulfide oxidation).

The Tt-associated gold observed in this study is common in chalcopryrite-lined conduits (Moss and Scott 2001; Wohlgemuth-Ueberwasser et al. 2015). Tennantite has been proposed to precipitate from high- $\alpha\text{S}_2$  conditions, which are also favorable for transporting Au (Hannington and Scott 1989; Vassileva et al. 2014). Since  $f_{\text{O}_2}$  increases and  $\alpha\text{S}_2$  decreases with the increasing degree of mixing between seawater and hydrothermal fluids (Haymon 1983), the Tt-associated gold is likely to be precipitated when  $\alpha\text{S}_2$  dropped during seawater ingression and the Au-bisulfide complex was destabilized with the precipitation of tennantite (Moss and Scott 2001). The Py-associated gold has been rarely observed in other seafloor hydrothermal sulfide precipitates (e.g., Ye et al. 2012) and is thought to precipitate during the mixing of high- and low-temperature hydrothermal fluids when both pH and  $f_{\text{O}_2}$  increase, leading to  $\text{H}_2\text{S}$  oxidation.

Gold has commonly been observed in massive sphalerite ( $>20\ \mu\text{m}$ ) in sulfide chimneys and the precipitation has been attributed to conductive cooling and mixing with seawater (Herzig et al. 1993; Hannington et al. 1995; Ye et al. 2012; Wu et al.

2016; Fuchs et al. 2019). Such gold occurs with anhedral shapes randomly in sphalerite, while, in our study, the Sp-associated gold occurs exclusively on the boundaries, forming chains of grains, at the epitaxial boundary from sphalerite to chalcopyrite, but is not observed in the late-stage massive sphalerite. Therefore, the Sp-associated gold is considered as a new type of gold occurrence in modern seafloor hydrothermal chimneys, distinct from previous occurrences in massive sphalerite. As discussed above, the particular phase transition is most likely to result from the overgrowth of chalcopyrite on sphalerite during the progressive mixing of hydrothermal fluid into seawater with increasing temperature. Such a fluid mixing process has been simulated by geochemical modeling with PACMANUS hydrothermal fluids in Fuchs et al. (2019). Modeling results show that the infiltration of hydrothermal fluids into seawater results in mineral precipitation in the following sequence: sphalerite → gold → chalcopyrite with increasing temperature, which is consistent with our observations. The discontinuous gold occurrence on the Sp 1 and chalcopyrite boundaries probably results from the partial dissolution of early sulfide and gold by new pulses of hot hydrothermal fluids.

The last type, Ccp-associated gold, exclusively occurs within cavities close to the interpreted dissolution and precipitation boundaries between Ccp 1 and 2 (Fig. 11). Although the occurrence of native gold in primary chalcopyrite has been frequently reported (e.g., Hannington et al. 1995; Herzig and Hannington 1995; Wu et al. 2016; Firstova et al. 2019; Fuchs et al. 2019), the gold-chalcopyrite association in this study has not been noticed before but is commonly observed in chimneys in PACMANUS hydrothermal field (Online Materials<sup>1</sup> Fig. S2). Gold occurs alongside fine-grained chalcopyrite within cavities located on the smooth boundaries of larger chalcopyrite grains (Fig. 11) and is interpreted to precipitate from fluid mixing when Au-rich fluids pass through the fractures of chalcopyrite.

However, the occurrence of nanoscale native gold observed in this study can be alternatively precipitated directly from colloidal gold transportation in venting fluids (Gartman et al. 2018; Falkenberg et al. 2021). Gold precipitated via colloidal transportation occurs as angular shapes filling in fractures or cavities in various minerals, which include chalcopyrite, pyrite, sphalerite and barite, whereas gold in this study presents unique spatial associations with various sulfides. Therefore, the colloidal transport mechanism is possibly responsible for the occurrence of native gold; however, fluid-seawater mixing mechanisms are more plausible on the basis of the textural evidence, as illustrated in this study. To probe the precise fluid mixing stages that lead to gold precipitation, further quantification by modeling is recommended.

### Growth model of the multiple conduits

Based on these new observations, in conjunction with published research on chimney growth (Haymon 1983; Koski et al. 1984; Butler and Nesbitt 1999; Berkenbosch et al. 2012), a detailed five-stage model accounting for the growth history of the observed multiple conduits, together with native gold precipitation, within a larger chimney structure, is proposed as follows (Fig. 12). Stage 1 includes the initially formed sulfate wall as soon as hydrothermal fluids come in contact with seawater, which, however, was dissolved during the continuing hydrothermal fluid flow. Sphalerite, gold, and chalcopyrite were gradually precipi-

tated during further fluid-seawater mixing at Stage 2. During this process, sphalerite was epitaxially overgrown by chalcopyrite with gold nanoparticles deposited on the boundaries (Fig. 12a). At Stage 3, the pyrite clusters, together with fine-grained gold, were precipitated when fluids flowed outward through the porous wall (Figs. 12b and 12c). Hot hydrothermal fluids passing through the wall caused the dissolution of sphalerite and precipitation of fine-grained chalcopyrite and sphalerite as well as the discontinuous occurrence of gold on the early sphalerite-chalcopyrite boundary. Chalcopyrite started to grow on the primary substrate outward, overgrowing pyrite clusters and thickening the wall. The pyrite-only wall of conduit 2 was precipitated in the nearby empty space (Fig. 12d), either from the diffused hydrothermal fluids forming conduit 1 or from a new pulse of venting fluid. The conduit walls of conduit 1 became less porous during Stage 4, and more chalcopyrite grew toward and away from the channel (Fig. 12f). The hydrothermal fluids also diffused to other empty space and mixed with low-temperature surrounding fluids, resulting in the precipitation of the chalcopyrite-only wall of the conduits 3 and 4. At the instant where two fluids met each other, the supersaturated conditions resulted in the formation of dendritic chalcopyrite (Fig. 12e). The fluxing of hot hydrothermal fluids is likely to dissolve the pre-existing chalcopyrite and sphalerite, and it will precipitate fine sulfide grains on the dissolved boundaries in region 3 of conduit 1. Native gold is precipitated exclusively in the cavities of chalcopyrite. Tennantite, together with native gold, was precipitated during the growth of the chalcopyrite wall. At the waning stage, like Stage 5, low-temperature galena, sphalerite, barite, and sometimes chalcocite were precipitated when the flux of hydrothermal fluids became weak and seawater entered (Figs. 12g and 12h).

### IMPLICATIONS

Seafloor hydrothermal chimneys from arcs and back-arc basins are enriched in Au with up to 56 ppm in bulk composition, but native gold is rarely observed, particularly in chalcopyrite-lined conduit walls (Moss and Scott 2001; Fuchs et al. 2019). In the eastern Manus Basin, a total of 303 native gold grains have been examined in four representative hydrothermal chimneys, and their occurrences were summarized in Moss and Scott (2001). The primary gold occurred as inclusions in tennantite and chalcopyrite and was interpreted to precipitate due to the decreased sulfur activity caused by fluid mixing or boiling. Gold is also observed to coexist with Bi-minerals (e.g., Bi telluride) in conduit walls of chimneys from Brothers volcanoes due to the involvement of magmatic fluids (Berkenbosch et al. 2012, 2019). Our study demonstrates that gold occurrence in the chalcopyrite-lined conduit walls is more variable than previously reported as it presents distinct associations with various sulfides, including chalcopyrite, sphalerite, and pyrite.

Furthermore, the Ccp-associated and Sp-associated gold (Figs. 5 and 7) were not reported before, although the chemical deposition mechanisms are similar to the published studies. Either Ccp-associated or Sp-associated gold was also exclusively observed within other chimneys. For example, the outer boundaries of chalcopyrite-lined conduit from another chimney contain Ccp-associated gold only where early-stage sphalerite is absent (Online Materials<sup>1</sup> Fig. S2). As interpreted above, both gold-sulfide associations form at different stages of the fluid mixing process.



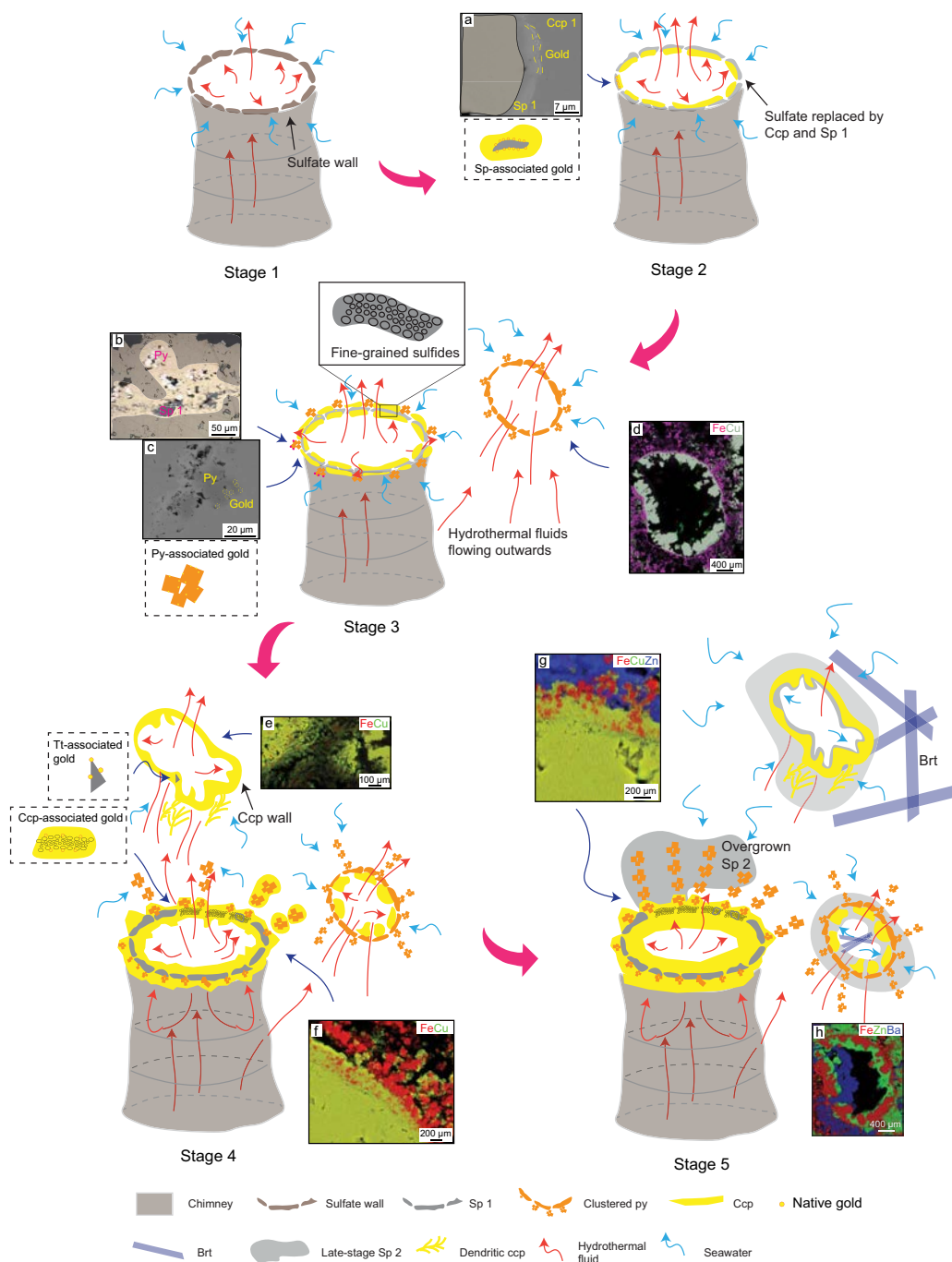


**FIGURE 12.** Proposed model of chimney growth. Stage 1: formation of a sulfate-dominated wall during the initial mixing of hydrothermal fluids and seawater. Stage 2: Sulfate was dissolved and replaced by sulfides, such as sphalerite (Sp 1) and chalcopyrite, during further fluids mixing. Sphalerite was overgrown epitaxially by chalcopyrite, corresponding to the BSE image showing that gold nanoparticles occurred as chains on the mineral boundaries (a). Stage 3: Hydrothermal fluids flowed away from the channel, resulting in the outgrowth of chalcopyrite and pyrite clusters in conduit 1, shown in b. Gold nanoparticles are also precipitated along with pyrite (c). The pluses of hydrothermal fluids caused the dissolution of chalcopyrite and precipitation of finer grained chalcopyrite, sphalerite and pyrite. Additional fluids flowed to the nearby empty space and formed a new conduit (conduit 2) with pyrite wall, as indicated in d. Stage 4: More hydrothermal fluids diffused to empty space and formed other conduits (3 and 4) with chalcopyrite-dominated wall, shown in e. The chalcopyrite wall of conduit 1 became thicker or more chalcopyrite overgrew pyrite clusters (f). During the development of the chalcopyrite wall, gold is deposited with tennantite. Chalcopyrite close to the porous Sp 1 layer in conduit 1 was dissolved and precipitated as fine-grained, during which Ccp-associated gold was precipitated. Stage 5: late-stage sphalerite (Sp 2) and barite (Brt) overgrew those chimneys, indicated by observations of (g and h) SXFM elemental map showing the late-stage sphalerite in h and barite in i overgrowing chalcopyrite and pyrite. (Color online.)

This implies that the broad spectrum of gold-sulfide associations can be variable among different chimneys, which are likely to be controlled by the various mixing process when hot hydrothermal fluids come in contact with surrounding fluids, together with magmatic contributions. The surrounding fluids can be either seawater or cooled hydrothermal fluids. This can be a new direction of searching for native gold in other modern and fossil chimneys, as well as ancient VMS deposits.

In the end, the combination of SXFM and EBSD analysis is demonstrated to be a useful approach to unraveling the paragenesis by mapping micrometer- to nanometer-scale mineralogical and microstructural features in regions of interest.

### ACKNOWLEDGMENTS

The authors acknowledge Editor Matthew Steele-MacInnis for handling the manuscript and two anonymous reviewers for insightful comments, which helped to improve the manuscript greatly. Mark Pearce, Weihua Liu, and Jessica Stromberg are thanked for insightful comments before manuscript submission.

### FUNDING

The authors acknowledge the support for SXFM work, which was undertaken on the X-ray fluorescence microscopy beamline at the Australian Synchrotron (Proposal 12589), part of Australia's Nuclear Science and Technology Organization (ANSTO). Chris Ryan and David Paterson are acknowledged for the assistance during data collection. S.H. and S.B. acknowledge the research-plus postdoctoral fellowship funded by the Commonwealth Science and Industry Research Organization (CSIRO).

### REFERENCES CITED

- Altree-Williams, A., Pring, A., Ngathai, Y., and Brugger, J. (2015) Textural and compositional complexities resulting from coupled dissolution-reprecipitation reactions in geomaterials. *Earth-Science Reviews*, 150, 628–651.
- Barrie, C.D., Boyce, A.J., Boyle, A.P., Williams, P.J., Blake, K., Wilkinson, J.J., Lowther, M., McDermott, P., and Prior, D.J. (2009) On the growth of colloform textures: a case study of sphalerite from the Galmoy ore body, Ireland. *Journal of the Geological Society*, 166, 563–582.
- Barrie, C.D., Boyle, A.P., Cook, N.J., and Prior, D.J. (2010) Pyrite deformation textures in the massive sulfide ore deposits of the Norwegian Caledonides. *Tectonophysics*, 483, 269–286.
- Barton, P.B., and Bethke, P.M. (1987) Chalcopyrite disease in sphalerite: Pathology and epidemiology. *American Mineralogist*, 72, 451–467.
- Benning, L., and Seward, T. (1996) Hydrosulfide complexing of Au (I) in hydrothermal solutions from 150–400°C and 500–1500 bars. *Geochimica et Cosmochimica Acta*, 60, 1849–1871.
- Berkenbosch, H.A., de Ronde, C.E.J., Gemmell, J.B., McNeill, A.W., and Goemann, K. (2012) Mineralogy and formation of black smoker chimneys from brothers submarine volcano, Kermadec Arc. *Economic Geology*, 107, 1613–1633.
- Berkenbosch, H.A., de Ronde, C.E.J., Ryan, C.G., McNeill, A.W., Howard, D.L., Gemmell, J.B., and Danyushevsky, L.V. (2019) Trace element mapping of copper- and zinc-rich black smoker chimneys from brothers volcano, kermadec arc, using synchrotron radiation XFM and LA-ICP-MS. *Economic Geology*, 114, 67–92.
- Binns, R.A. (2014) Birkpela: A large siliceous chimney from the PACMANUS hydrothermal field, Manus basin, Papua New Guinea. *Economic Geology*, 109, 2243–2259.
- Binns, R.A., and Scott, S.D. (1993) Actively forming polymetallic sulfide deposits associated with felsic volcanic rocks in the Eastern Manus Back-Arc Basin, Papua New Guinea. *Economic Geology*, 88, 2226–2236.
- Binns, R.A., Parr, J.M., Scott, S.D., Gemmell, J.B., and Herzig, P.M. (1995) PACMANUS: An active seafloor hydrothermal field on siliceous volcanics in rocks of the eastern Manus Basin. *Papue New Guinea. PACRIM*, 95, 49–54.
- Binns, R.A., Barriga, F.J.A.S., and Miller, D.J. (2007) Leg 193 Synthesis: Anatomy of an active felsic-hosted hydrothermal system, Eastern Manus Basin, Papua New Guinea. *Proceedings of the Ocean Drilling Program, Scientific Results*, 193, 1–71.
- Butler, I.B., and Nesbitt, R.W. (1999) Trace element distributions in the chalcopyrite wall of a black smoker chimney: Insights from laser ablation inductively coupled plasma mass spectrometry (LA-ICP-MS). *Earth and Planetary Science Letters*, 167, 335–345.
- Davies, H.L., Honza, E., Tiffin, D.L., Lock, J., Okuda, Y., Keene, J.B., Murakami, F., and Kisimoto, K. (1987) Regional setting and structure of the western Solomon Sea. *Geo-Marine Letters*, 7, 153–160.
- de Ronde, C.E.J., Faure, K., Bray, C.J., Chappell, D.A., and Wright, I.C. (2003) Hydrothermal fluids associated with seafloor mineralization at two southern Kermadec arc volcanoes, offshore New Zealand. *Mineralium Deposita*, 38, 217–233.
- de Ronde, C.E.J., Hannington, M.D., Stoffers, P., Wright, I.C., Ditchburn, R.G., Reyes, A.G., Baker, E.T., Massoth, G.J., Lupton, J.E., Walker, S.L., and others. (2005) Evolution of a submarine magmatic-hydrothermal system: Brothers volcano, southern Kermadec Arc, New Zealand. *Economic Geology*, 100, 1097–1133.
- de Ronde, C.E.J., Massoth, G.J., Butterfield, D.A., Christenson, B.W., Ishibashi, J., Ditchburn, R.G., Hannington, M.D., Brathwaite, R.L., Lupton, J.E., Kamenetsky, V.S., and others. (2011) Submarine hydrothermal activity and gold-rich mineralization at Brothers Volcano, Kermadec Arc, New Zealand. *Mineralium Deposita*, 46, 541–584.
- Deditius, A.P., Utsunomiya, S., Renock, D., Ewing, R.C., Ramana, C.V., Becker, U., and Kesler, S.E. (2008) A proposed new type of arsenian pyrite: Composition, nanostructure and geological significance. *Geochimica et Cosmochimica Acta*, 72, 2919–2933.
- Dekov, V.M., Rouxel, O., Kouzmanov, K., Bindi, L., Asael, D., Fouquet, Y., Etoubeau, J., Burgaud, G., and Wälle, M. (2016) Enargite-luzonite hydrothermal vents in Manus Back-Arc Basin: Submarine analogues of high-sulfidation epithermal mineralization. *Chemical Geology*, 438, 36–57.
- Etschmann, B., Brugger, J., Pearce, M.A., Ta, C., Brautigan, D., Jung, M., and Pring, A. (2014) Grain boundaries as microreactors during reactive fluid flow: Experimental dolomitization of a calcite marble. *Contributions to Mineralogy and Petrology*, 168, 1–12.
- Falkenberg, J.J., Keith, M., Haase, K.M., Bach, W., Klemm, R., Strauss, H., Yeo, I.A., Rubin, K.H., Storch, B., and Anderson, M.O. (2021) Effects of fluid boiling on Au and volatile element enrichment in submarine arc-related hydrothermal systems. *Geochimica et Cosmochimica Acta*, 307, 105–132.
- Firstova, A., Stepanova, T., Sukhanova, A., Cherkashov, G., and Poroshina, I. (2019) Au and Te minerals in seafloor massive sulphides from seymenov-2 hydrothermal field, mid-atlantic ridge. *Minerals*, 9, 294.
- Fisher, L.A., Fougereuse, D., Cleverley, J.S., Ryan, C.G., Mickelthwaite, S., Halfpenny, A., Hough, R.M., Gee, M., Paterson, D., Howard, D.L., and Spiers, K. (2015) Quantified, multi-scale X-ray fluorescence element mapping using the Maia detector array: Application to mineral deposit studies. *Mineralium Deposita*, 50, 665–674.
- Franklin, J., Gibson, H., Jonasson, I., and Galley, A. (2005) Volcanogenic massive sulfide deposits. *Economic Geology*, 100th Anniversary Volume, 523–560.
- Freitag, K., Boyle, A.P., Nelson, E., Hitzman, M., Churchill, J., and Lopez-Pedrosa, M. (2004) The use of electron backscatter diffraction and orientation contrast imaging as tools for sulphide textural studies: Example from the Greens Creek deposit (Alaska). *Mineralium Deposita*, 39, 103–113.
- Fuchs, S., Hannington, M.D., and Petersen, S. (2019) Divining gold in seafloor polymetallic massive sulfide systems. *Mineralium Deposita*, 54, 789–820.
- Gartman, A., Hannington, M., Jamieson, J.W., Peterkin, B., Garbe-Schönberg, D., Findlay, A.J., Fuchs, S., and Kwasnitschka, T. (2018) Boiling-induced formation of colloidal gold in black smoker hydrothermal fluids. *Geology*, 46, 39–42.
- Gena, K. (2013) Deep sea mining of submarine hydrothermal deposits and its possible environmental impact in Manus Basin, Papua New Guinea. *Procedia Earth and Planetary Science*, 6, 226–233.
- German, C.R., and Seyfried, W.E. (2014) Hydrothermal processes. In H.D. Holland and K.K. Turekian, Eds., *The Oceans and Marine Geochemistry*, 8, pp. 191–233. Elsevier.
- Glenn, M., Hu, S., Barnes, S., Torpy, A., Hughes, A.E., MacRae, C.M., Webster, N.A.S., Wilson, N.C., Parr, J., and Binns, R. (2020) Investigation of the internal structure of a modern seafloor hydrothermal chimney with a combination of EBSD, EPMA, and XRD. *Microscopy and Microanalysis: The Official Journal of Microscopy Society of America, Microbeam Analysis Society, Microscopical Society of Canada*, 26, 793–715.
- Halbach, P., Blum, N., Münch, U., Plüger, W., Garbe-Schönberg, D., and Zimmer, M. (1998) Formation and decay of a modern massive sulfide deposit in the Indian Ocean. *Mineralium Deposita*, 33, 302–309.
- Hannington, M.D., and Scott, S.D. (1989) Sulfidation equilibria as guides to gold mineralization in volcanogenic massive sulfides: Evidence from sulfide mineralogy and the composition of sphalerite. *Economic Geology*, 84, 1978–1995.
- Hannington, M.D., Peter, J.M., and Scott, S.D. (1986) Gold in sea floor polymetallic sulfide deposits. *Economic Geology*, 81, 1867–1883.
- Hannington, M., Herzig, P., Scott, S., Thompson, G., and Rona, P. (1991) Comparative mineralogy and geochemistry of gold-bearing sulfide deposits on the mid-ocean ridges. *Marine Geology*, 101, 217–248.
- Hannington, M.D., Tivey, M.K., Larocque, A.C.L., and Petersen, S., and Rona, P.A. (1995) The occurrence of gold in sulfide deposits of the TAG hydrothermal field, Mid-Atlantic Ridge. *Canadian Mineralogist*, 33, 1285–1310.
- Hannington, M.D., de Ronde, C.E.J., and Petersen, S. (2005) Sea-floor tectonics and submarine hydrothermal systems. *Economic Geology*, 100th Anniversary Volume, 111–141.
- Haymon, R.M. (1983) Growth history of hydrothermal black smoker chimneys. *Nature*, 301, 695–698.
- Haymon, R.M., and Kastner, M. (1981) Hot spring deposits on the East Pacific Rise at 21°N: preliminary description of mineralogy and genesis. *Earth and Planetary Science Letters*, 53, 363–381.
- Haymon, R.M., Fornari, D.J., Edwards, M.H., Carbotte, S., Wright, D., and Macdonald, K.C. (1991) Hydrothermal vent distribution along the East Pacific Rise crest (9°09'–54°N) and its relationship to magmatic and tectonic processes on fast-spreading mid-ocean ridges. *Earth and Planetary Science Letters*, 104, 513–534.
- Herzig, P.M., and Hannington, M.D. (1995) Polymetallic massive sulfides at the modern



- seafloor, a review. *Ore Geology Reviews*, 10, 95–115.
- Herzig, P.M., Hannington, M.D., Fouquet, Y., Von Stackelberg, U., and Petersen, S. (1993) Gold-rich polymetallic sulfides from the Izu back arc and implications for the geochemistry of gold in seafloor hydrothermal systems of the Southwest Pacific. *Economic Geology*, 88, 2182–2209.
- Hu, S.-Y., Barnes, S.J., Glenn, A.M., Pagès, A., Parr, J., MacRae, C., and Binns, R. (2019) Growth history of sphalerite in a modern sea floor hydrothermal chimney revealed by electron backscattered diffraction. *Economic Geology*, 114, 165–176.
- Hu, S.-Y., Barnes, S.J., Pagès, A., Parr, J., Binns, R., Verrall, M., Quadir, Z., Rickard, W.D.A., Liu, W., Fougereuse, D., and others. (2020) Life on the edge: Microbial biomineralization in an arsenic- and lead-rich deep-sea hydrothermal vent. *Chemical Geology*, 533, 119438.
- Hu, S.Y., Evans, K., Fisher, L., Rempel, K., Craw, D., Evans, N.J., Cumberland, S., Robert, A., and Grice, K. (2016) Associations between sulfides, carbonaceous material, gold and other trace elements in polyframboids: Implications for the source of orogenic gold deposits, Otago Schist, New Zealand. *Geochimica et Cosmochimica Acta*, 180, 197–213.
- Iizasa, K., Asada, A., Mizuno, K., Katase, F., Lee, S., Kojima, M., and Ogawa, N. (2018) Native gold and gold-rich sulfide deposits in a submarine basaltic caldera, Higashi-Aogashima hydrothermal field, Izu-Ogasawara frontal arc. *Japan. Mineralium Deposita*, 1–16.
- Janecky, D.R., and Seyfried, W.E. (1984) Formation of massive sulfide deposits on oceanic ridge crests: Incremental reaction models for mixing between hydrothermal solutions and seawater. *Geochimica et Cosmochimica Acta*, 48, 2723–2738.
- Kamenetsky, V.S., Binns, R.A., Gemmell, J.B., Crawford, A.J., Memagh, T.P., Maas, R., and Steele, D. (2001) Parental basaltic melts and fluids in eastern Manus back-arc Basin: Implications for hydrothermal mineralization. *Earth and Planetary Science Letters*, 184, 685–702.
- Keith, M., Haase, K.M., Schwarz-Schampera, U., Klemm, R., Petersen, S., and Bach, W. (2014) Effects of temperature, sulfur, and oxygen fugacity on the composition of sphalerite from submarine hydrothermal vents. *Geology*, 42, 699–702.
- Kojima, S., and Sugaki, A. (1987) An experimental study on chalcopyritization of sphalerite induced by hydrothermally metasomatic reactions. *Mining Geology*, 37, 373–380.
- Koski, R.A., Clague, D.A., and Oudin, E. (1984) Mineralogy and chemistry of massive sulfide deposits from the Juan de Fuca Ridge. *Geological Society of America Bulletin*, 95, 930–945.
- Koski, R.A., Jonasson, I.R., Kadko, D.C., Smith, V.K., and Wong, F.L. (1994) Compositions, growth mechanisms, and temporal relations of hydrothermal sulfide-sulfate-silica chimneys at the northern Cleft segment, Juan de Fuca Ridge. *Journal of Geophysical Research: Solid Earth*, 99, 4813–4832.
- Kristall, B., Kelley, D.S., Hannington, M.D., and Delaney, J.R. (2006) Growth history of a diffusely venting sulfide structure from the Juan de Fuca Ridge: A petrological and geochemical study. *Geochimica, Geophysics, Geosystems*, 7, Q07001, doi: 10.1029/2005GC001166.
- Kristall, B., Nielsen, D., Hannington, M.D., Kelley, D.S., and Delaney, J.R. (2011) Chemical microenvironments within sulfide structures from the Mofu Hydrothermal Field: Evidence from high-resolution zoning of trace elements. *Chemical Geology*, 290, 12–30.
- Maitland, T., and Sitzman, S. (2007) EBSD technique and materials characterization. in *scanning microscopy for nanotechnology. Techniques and Applications*, 41–76.
- Martinez, F., and Taylor, B. (1996) Backarc spreading, rifting, and microplate rotation, between transform faults in the Manus Basin. *Marine Geophysical Researches*, 18, 203–224.
- Meier, D.V., Pjévac, P., Bach, W., Markert, S., Schweder, T., Jamieson, J., Petersen, S., Amann, R., and Meyerdiérs, A. (2019) Microbial metal-sulfide oxidation in inactive hydrothermal vent chimneys suggested by metagenomic and metaproteomic analyses. *Environmental Microbiology*, 21, 682–701.
- Moss, R., and Scott, S.D. (2001) Geochemistry and mineralogy of gold-rich hydrothermal precipitates from Eastern Manus Basin, Papua New Guinea. *Canadian Mineralogist*, 39, 957–978.
- Murphy, P.J., and Meyer, G. (1998) A Cu-Au association in ultramafic hosted hydrothermal sulfide. *Economic Geology*, 93, 1076–1083.
- Nozaki, T., Ishibashi, J.-I., Shimada, K., Nagase, T., Takaya, Y., Kato, Y., Kawagucci, S., Watsui, T., Shibuya, T., Yamada, R., and others. (2016) Rapid growth of mineral deposits at artificial seafloor hydrothermal vents. *Scientific Reports*, 6, 22163.
- Pašava, J., Vymazalová, A., Petersen, S., and Herzig, P. (2004) PGE distribution in massive sulfides from the PACMANUS hydrothermal field, eastern Manus basin, Papua New Guinea: Implications for PGE enrichment in some ancient volcanogenic massive sulfide deposits. *Mineralium Deposita*, 39, 784–792.
- Paterson, D., De Jonge, M.D., Howard, D.L., Lewis, W., McKinlay, J., Starritt, A., Kusel, M., Ryan, C.G., Kirkham, R., and Moorhead, G. and others. (2011) The X-ray fluorescence microscopy beamline at the Australian synchrotron. In *AIP Conference Proceedings*, vol. 1365, p. 219–222.
- Pearce, M.A., Timms, N.E., Hough, R.M., and Cleverley, J.S. (2013) Reaction mechanism for the replacement of calcite by dolomite and siderite: Implications for geochemistry, microstructure and porosity evolution during hydrothermal mineralization. *Contributions to Mineralogy and Petrology*, 166, 995–1009.
- Petersen, S., Lehmann, B., and Murton, B.J. (2018) Modern seafloor hydrothermal systems: New perspectives on ancient ore-forming processes. *Elements*, 14, 307–312.
- Putnis, A. (2009) Mineral replacement reactions. *Reviews in Mineralogy and Geochemistry*, 70, 87–124.
- Reeves, E.P., Seewald, J.S., Saccoccia, P., Bach, W., Craddock, P.R., Shanks, W.C., Sylva, S.P., Walsh, E., Pichler, T., and Rosner, M. (2011) Geochemistry of hydrothermal fluids from the PACMANUS, Northeast Pual and Vienna Woods hydrothermal fields, Manus Basin, Papua New Guinea. *Geochimica et Cosmochimica Acta*, 75, 1088–1123.
- Reeves, E.P., Yoshinaga, M.Y., Pjévac, P., Goldenstein, N.I., Peplies, J., Meyerdiérs, A., Amann, R., Bach, W., and Hinrichs, K.U. (2014) Microbial lipids reveal carbon assimilation patterns on hydrothermal sulfide chimneys. *Environmental Microbiology*, 16, 3515–3532.
- Rona, P.A., Klinkhammer, G., Nelsen, T.A., Trefry, J.H., and Elderfield, H. (1986) Black smokers, massive sulphides and vent biota at the Mid-Atlantic ridge. *Nature*, 321, 33–37.
- Ryan, C.G., Kirkham, R., Hough, R.M., Moorhead, G., Siddons, D.P., de Jonge, M.D., Paterson, D.J., De Geronimo, G., Howard, D.L., and Cleverley, J.S. (2010a) Elemental X-ray imaging using the Maia detector array: The benefits and challenges of large solid-angle. *Nuclear Instruments and Methods in Physics Research, Section A: Accelerators, Spectrometers, Detectors and Associated Equipment*, 619, 37–43.
- Ryan, C.G., Siddons, D.P., Kirkham, R., Dunn, P.A., Kuczewski, A., Moorhead, G., De Geronimo, G., Paterson, D.J., De Jonge, M.D., Hough, R.M., and others. (2010b) The new Maia detector system: Methods for high-definition trace element imaging of natural material. *AIP Conference Proceedings*, 1221, 9–17.
- Ryan, C.G., Siddons, D.P., Kirkham, R., Li, Z.Y., de Jonge, M.D., Paterson, D., Cleverley, J.S., Kuczewski, A., Dunn, P.A., Jensen, M. and others (2013) The Maia detector array and X-ray fluorescence imaging system: locating rare precious metal phases in complex samples. *Proceedings of SPIE*, 8851, 88510Q.
- Ryan, C.G., Siddons, D.P., Kirkham, R., Li, Z.Y., de Jonge, M.D., Paterson, D.J., Kuczewski, A., Howard, D.L., Dunn, P.A., Falkenberg, G., and others. (2014) Maia X-ray fluorescence imaging: Capturing detail in complex natural samples. *Journal of Physics: Conference Series*, 499, 012002.
- Stefánsson, A., and Seward, T.M. (2003) Experimental determination of the stability and stoichiometry of sulphide complexes of silver(I) in hydrothermal solutions to 400 °C. *Geochimica et Cosmochimica Acta*, 67, 1395–1413.
- (2004) Gold(I) complexing in aqueous sulphide solutions to 500 °C at 500 bar. *Geochimica et Cosmochimica Acta*, 68, 4121–4143.
- Tao, C., Lin, J., Guo, S., Chen, Y.J., Wu, G., Han, X., German, C.R., Yoerger, D.R., Zhou, N., Li, H., Su, X., and Zhu, J. and the DY115-19 (Legs 1–2) and DY115-20 (Legs 4–7) Science Parties. (2012) First active hydrothermal vents on an ultraslow-spreading center: Southwest Indian Ridge. *Geology*, 40, 47–50.
- Taylor, B. (1979) Bismarck Sea: Evolution of a back-arc basin. *Geology*, 7, 171–174.
- Törmänen, T.O., and Koski, R.A. (2005) Gold enrichment and the Bi-Au association in pyrrhotite-rich massive sulfide deposits, Escanaba trough, Southern Gorda Ridge. *Economic Geology*, 100, 1135–1150.
- Tregoning, P. (2002) Plate kinematics in the western Pacific derived from geodetic observations. *Journal of Geophysical Research: Solid Earth*, 107, ECV 7-1–ECV 7-8.
- Turner, J.S., and Campbell, I.H. (1987) A laboratory and theoretical study of the growth of “black smoker” chimneys. *Earth and Planetary Science Letters*, 82, 36–48.
- Vassileva, R.D., Atanasova, R., and Kouzmanov, K. (2014) Tennantite-tetrahedrite series from the Madan Pb-Zn deposits, Central Rhodopes, Bulgaria. *Mineralogy and Petrology*, 108, 515–531.
- Williams-Jones, A.E., Bowtell, R.J., and Migdisov, A.A. (2009) Gold in solution. *Elements*, 5, 281–287.
- Wohlgemuth-Ueberwasser, C.C., Viljoen, F., Petersen, S., and Vorster, C. (2015) Distribution and solubility limits of trace elements in hydrothermal black smoker sulfides: An in-situ LA-ICP-MS study. *Geochimica et Cosmochimica Acta*, 159, 16–41.
- Wu, Z., Sun, X., Xu, H., Konishi, H., Wang, Y., Wang, C., Dai, Y., Deng, X., and Yu, M. (2016) Occurrences and distribution of “invisible” precious metals in sulfide deposits from the Edmond hydrothermal field, Central Indian Ridge. *Ore Geology Reviews*, 79, 105–132.
- Ye, J., Shi, X., Yang, Y., Li, N., Liu, J., and Su, W. (2012) The occurrence of gold in hydrothermal sulfide at Southwest Indian Ridge 49.6° E. *Acta Oceanologica Sinica*, 31, 72–82.
- Yeats, C.J., Hollis, S.P., Halfpenny, A., Corona, J.C., LaFlamme, C., Southam, G., Fiorentini, M., Herrington, R.J., and Spratt, J. (2017) Actively forming Kuruko-type volcanic hosted massive sulfide (VHMS) mineralization at Iheya North, Okinawa Trough, Japan. *Ore Geology Reviews*, 84, 20–41.

MANUSCRIPT RECEIVED OCTOBER 22, 2020

MANUSCRIPT ACCEPTED JULY 29, 2021

MANUSCRIPT HANDLED BY MATTHEW STEELE-MACINNIS

## Endnote:

<sup>1</sup>Deposit item AM-22-87866, Online Materials. Deposit items are free to all readers and found on the MSA website, via the specific issue's Table of Contents (go to [http://www.minsocam.org/MSA/AmMin/TOC/2022/Aug2022\\_data/Aug2022\\_data.html](http://www.minsocam.org/MSA/AmMin/TOC/2022/Aug2022_data/Aug2022_data.html)).